

Impact Modification of Mercury's Mantle Composition

by

Sean M. Wahl

Submitted to the Department of Earth, Atmospheric and Planetary
Science

in partial fulfillment of the requirements for the degree of

Bachelor of Science in Earth, Atmospheric and Planetary Science

at the

MASSACHUSETTS INSTITUTE OF TECHNOLOGY

May 2011

©Copyright 2011 Sean M. Wahl All rights reserved.

The author hereby grants to MIT permission to reproduce and to
distribute publicly paper and electronic copies of this thesis document
in whole or in part in any medium now known or hereafter created.

Author
Sean M. Wahl

Department of Earth and Planetary Science, Department of Physics
May 6, 2011

Certified by
Linda T. Elkins-Tanton
Assistant Professor of Geology
Thesis Supervisor

Accepted by
Samuel Bowring
Chair, Committee on Undergraduate Program

Impact Modification of Mercury's Mantle Composition

by

Sean M. Wahl

Submitted to the Department of Earth, Atmospheric and Planetary Science
on May 6, 2011, in partial fulfillment of the
requirements for the degree of
Bachelor of Science in Earth, Atmospheric and Planetary Science

Abstract

Difficulties encountered in reproducing Mercury's compositional attributes through modeling of formational processes have bolstered support for the hypothesis that one or more giant impacts stripped away a significant proportion of proto-Mercury's silicate mantle. Previous investigations demonstrate sufficient removal of mantle material to account for the planets unusually high mean density, but do not consider the effects of multiple silicate and oxide phases. In this study, we extend the present theory by investigating the consequences of a more realistic chemical model on the evolution of the ejected material. We suggest that the majority of condensation within the expanding vapor plume can be modeled as an equilibrium process following homogeneous nucleation of refractory phases leading to larger particle sizes than previously estimated. We use a thermodynamic model focused on major element composition of ejected material to analyze the effect of differential condensation on the expansion and final state of ejecta. We also adapt pre-existing models for chemistry of condensation and impact shock compression to address additional problems associated with the process. For ejecta of sufficiently high specific entropy, our simplified chemical models indicate that energy released during condensation of *MgO*-rich phases buffers the temperature, delaying or preventing onset of *FeO* condensation. If sufficient spatial separation between condensates and vapor arises or if significant amounts of uncondensed *FeO* vapor remain uncondensed, reaccumulated ejecta would be enriched in *MgO* and refractory phases. This is compatible with an *FeO* depletion of Mercurys surface relative to other terrestrial bodies as some spectroscopic data suggests. The proposed process leads to a greater depletion in *FeO* and a lesser depletion in refractory, incompatible elements (Al_2O_3 , *CaO*, *TiO_2*), than models assuming uniform removal of material from a differentiated proto-Mercury.

Thesis Supervisor: Linda T. Elkins-Tanton
Title: Assistant Professor of Geology

Acknowledgments

I would like to acknowledge David J. Stevenson (Caltech) for supervising the initial research as a part of Caltech's SURF program, Sarah T. Stewart-Mukhopadhyay (Harvard) for her discussion and help finding the necessary resources for this project and Thomas Herring for help with programming. I would also like to thank Mark Ghiorso (of the University of Washington) and Ebel Ghiorso (of the American Museum of Natural History), for their discussion regarding chemical models.

CONTENTS

I. Introduction	10
I.1. Formation of Mercury	10
I.2. Giant Impacts and Inner Solar System Evolution	11
I.3. Collisional Stripping of Mantle Material	12
I.4. Motivation from Spectroscopic Data	13
I.5. Moment of Inertia	14
II. Proposed Scenario	16
II.1. Initial Conditions and ‘Parcel’ Method	16
II.2. Homogeneous Condensation	17
II.3. Equilibrium Condensation	18
II.4. Removal Versus Reaccretion of Ejected Material	19
II.5. ‘Road Map’	19
III. Vapor Production	20
III.1. Shock Compression	20
III.2. Semi-Analytic Methods	21
III.3. Impedence Matching Technique	22
III.4. Experiment Versus Modelling	23
III.5. Vapor Production Results	23
IV. Modeling the Expanding Vapor Plume	30
IV.1. Thermodynamic Model	30
IV.2. Computational Methods	31
IV.3. Results	34
V. Discussion	41
V.1. Motivation and Constraints from Modeled Vapor Production	41
V.2. Iron-Magnesium Differentiation by the Expanding Vapor Plume	43
V.3. Unexplored Parameters	45
V.4. Future Work	47

VI. Conclusion	49
A. Coupling of Vapor and Liquid Droplets	49
B. Equilibrium Criterion	50
C. Removal Timescales	51
References	53

LIST OF FIGURES

1	Olivine Hugoniot and liquid-vapor phase boundary	25
2	Impedance matching technique with olivine Hugoniot for various impact ve- locities	26
3	Decompression adiabats and liquid-vapor phase boundaries	26
4	Effect of impactor velocity on vapor productions	27
5	Effect of impactor mass on vapor productions	27
6	Conditions for incipient condensation for modeled liquid phases	38
7	Thermodynamic path for representative vapor plume simulation	38
8	Fraction of Mg condensed for representative vapor plume simulation	39
9	The effect of initial specific entropy on the thermodynamic path of expansion	39
10	Predicted conditions of incipient forsterite condensation for released vapor from isobaric cores	40
11	The effect of initial specific entropy on the thermodynamic path of expansion	40

LIST OF TABLES

I	Physical properties of the terrestrial planets and their Cores	15
II	Motivating results of SPH simulations by Benz et. al. 2007	15
III	Estimates for vapor production using the semi-analytic methods I	28
IV	Estimates for vapor production using the semi-analytic methods II	29
V	Thermodynamic parameters of modeled liquid and vapor phases	37
VI	Range of conditions for which Fe-Mg fractionation is predicted	37

I. INTRODUCTION

I.1. Formation of Mercury

As NASA’s MESSENGER probe prepares for its insertion into Mercury’s orbit, the promise of abundant new data, including spectroscopic analysis of surface composition and better geophysical constraints for the planet’s interior structure, has sparked increased interest in the least-studied terrestrial planet. One outstanding problem is Mercury’s unusually high mean density (see Table I); the uncompressed density of Mercury is 5.3 g/cm^3 , compared to Earth’s 4.04 g/cm^3 [17], indicating that Mercury has a large reduced-iron-rich core in comparison to its silicate mantle. It is generally agreed that the cause of this anomalously high mean density is the result of iron-Silicate differentiation early in Mercury’s history [5, 6, 8, 19, 28, 29, 58]. The circumstances under which this differentiation took place, however, have been the subject of an unresolved debate for decades. Hypotheses include fractionation during condensation from the planetary nebula [28, 29, 58] as well as during the partial vaporization and removal of Mercury’s rocky mantle by strong nebular winds in the early nebula [8, 19].

The Lewis hypothesis makes use of a radial temperature gradient in the proto-planetary disk, to produce a trend of increasingly refractory dominant compositions with decreasing distance from the sun. In this case, proto-Mercury’s location at the time of accretion would be in a part of the disk with a temperature high enough such that metallic iron condensation would be nearly complete, while forsterite would remain partially condensed. Predictions of nebular condensation temperatures [31] demonstrate that the thermodynamic phase-space over which such differentiation could occur is quite narrow. As a result, the scenario put forward by Lewis requires an unrealistically stable temperature gradient to for proto-Mercury to remain under the correct conditions for the majority of its condensation.

Weidenschilling 1978 [58] looks at the effect of ongoing accretion in the gas rich proto-planetary disk. Gas drag would cause decay of the orbits of particles, with more massive, denser particles decaying less rapidly. The calculations presented in the paper suggest that this would lead to an enrichment of iron rich condensates in the remaining material at Mercury’s orbit prior to the bulk of the planet’s accretion. This theory has the added benefit of retaining siderophile elements, particularly sulfur, which are often invoked in

explaining Mercury’s apparently liquid outer core [32, 53]. While the model does lead to iron enrichment on the scale necessary to recreate Mercury’s iron to silicate ratio ratio, it has difficulty explaining compositional trends not affected by large density disparities and relies on a variety of ad hoc assumptions about conditions within the disk to reach the correct value.

The hypotheses of Lewis and Weidenschilling both suffer from their reliance on processes restricted to early, gas-rich stages of condensation and accretion in the proto-planetary disk. During these early stages of accretion, the radial motions of the largest planetesimals are damped by gas drag and dynamic friction [11], thus, accretion of bodies tends to be restricted to isolated feeding zones. However, once the system becomes dominated by a smaller number of more massive planetary embryos, the system becomes chaotic and planetesimals traverse the entirety of the inner solar system, mixing together any distinct condensates that may have formed at different radii in the disk. Assuming that N-body simulations [10, 12] accurately model the late stage accretion, a large anomaly in density is unlikely to survive.

Another popular theory focusing on events after the majority of condensation has occurred is the possibility that a significant portion of Mercury’s mantle was vaporized by an intense radiation and solar wind from the young sun [8, 19]. It is unclear, however, that the necessary stellar conditions [47] to remove matter at a sufficient rate would have coexisted or postdated the late stages of planetary accretion. A more plausible proposal is differentiation due to the ejection and subsequent removal of proto-Mercury mantle as a result of one or more major impacts [5] .

I.2. Giant Impacts and Inner Solar System Evolution

Impacts played a major role in shaping the inner solar system of today. In addition to being the primary cause of surface features on most rocky bodies, an impact related origin has been suggested for a variety of seemingly unique planetary features. Among the most prevalent are: the crustal dichotomy on Mars [3, 20, 33], Venus’ slow, retrograde rotation [2] and the formation of the Earth’s Moon [9]. Any such large scale impact would date back to the last major phase of planetary accretion [11]. In dynamical simulations of this period, a relatively small number of planetary embryos excite one another’s orbits, causing the final mixing and merging of bodies, of which then resulted in the terrestrial planets we see today

are composed.

I.3. Collisional Stripping of Mantle Material

Benz et. al 2007 [6] (along with [5] and [4]) presents a tentative explanation for the high mean density as a result of a major impact on an approximately Mars-sized proto-Mercury. Their work utilizes smooth-particle hydrodynamic (SPH) simulations to model the impact and reformation to determine the source and amount of material ejected. The same authors then use hydrodynamic theory to estimate the size of particles formed by the cooling ejecta, the determining factor in how rapidly material is removed from Mercury crossing orbits.

What has yet to be considered in detail is the effect that the aftermath of such an impact would have on a multi-phase silicate mantle. More complex considerations of the chemistry of the ejecta plume are necessary in order to create testable hypotheses, by which a giant impact might be identified as a dominant process in Mercury's evolution. Mercury's present day core size is a non-unique result with respect to various proposed mechanisms. However, these hypotheses may be distinguishable with a better understanding of their effect on mantle and crustal composition. Benz's paper presents results of SPH simulations of impacts on a proto-mercury with a similar size core, surrounded by a larger silicate mantle such that the iron to silicate ratio is $\sim .5$ by mass or ~ 1.3 by number. They choose a range of parameters for their impactor varying the relative velocity from 20-30 km/s, an impact parameter varying from 0-.7 and an impactor to target mass ratio ranging from .1-.2. While not an exhaustive search through the potential parameters, these represent a range that is plausible for impacts occurring at Mercury's orbital radius during the late stages of planetary accretion. Since this range of energetic impacts has been shown to recreate final planets with masses and iron to silicate ratios similar to that of Mercury, it is this range which we focus upon here. Table II presents the parameters and results of the simulations from Benz et. al. 2007 [6] that produce a final planet most similar to present day Mercury. The simulations also place an approximate upper limit on these parameters, as sufficient mass or impact velocity lead to disruption of the target.

I.4. Motivation from Spectroscopic Data

The ultimate goal of this type of research is to identify criteria by which the results of an impact dominated evolution can be distinguished from other origin hypotheses. Such a criteria would likely involve comparing spectroscopic observations of the planet’s surface to predicted compositions from formational models. Here we highlight various spectroscopic data of Mercury’s surface which may be relevant to the story of the planet’s formation. There are some apparent contradictions between such data derived from different techniques, which may be cleared up with better data from the orbital phase of MESSENGER’s mission.

There are no known samples of Mercury’s surface, and the surface has never been visited by any probe. It has been suggested that Mercury might be the parent body of a class of meteorite called the angrites [24]. The evidence for this rests largely on the absence of volatiles such as sodium in the angrites, and can not be uniquely linked to Mercury without comparison with actual Mercurian samples. There is arguably stronger evidence against angrites being from Mercury, most notably that the spectral properties of angrite samples do not match any measurements of Mercury’s surface [23]. Because of the gravitational energy that must be overcome to move material from Mercury’s orbit, such meteorite falls are expected to be exceedingly rare in comparison.

One of the objectives that the MESSENGER mission hopes to accomplish is to determine the abundance of iron on the planet’s surface. To date this aspect has been made more uncertain by conflicting inferences made by different spectroscopic techniques. A variety of spectroscopic studies indicate significant depletion of the silicate surface material in FeO in comparison to other terrestrial bodies [16, 54]. This view is drawn largely from Earth based visible, infrared and microwave spectroscopy [25, 40, 57], as well as color analysis [50] and albedo [15] of images taken by the Mariner 10 spacecraft. Perhaps the most convincing constraint is the complete absence of an absorption feature at $1\ \mu\text{m}$. This feature is diagnostic of Fe^{2+} in silicate material, and its absence is generally taken to indicate <3 wt. % iron in silicates exposed at the surface [34]. Although this is the state of iron typically observed on planetary surfaces, the absence of a $1\ \mu\text{m}$ feature does not necessarily rule out iron in a different phase or oxidation state.

One ne simple petrologic explanation for such an absence of FeO in surface silicates is an FeO-poor source material, since the solid-melt partition coefficient is approximately unity

[50]. This is likely not a unique solution, but we take this as sufficient evidence to warrant considerations for how impact related processes might deplete bulk-mantle FeO. It should be noted that a popular, competing hypothesis is that the surface lacks basalt, igneous deposits resulting from melting of the mantle [25]. If this is the case, inferring bulk-mantle compositions from surface compositions would be particularly difficult. A more complete comparison of geological features to higher resolution spectral analysis by MESSENGER may help in determining which, if either, of these petrologic interpretations is correct.

Near-infrared and ultraviolet [34] spectral analysis from MESSENGER's initial flyby supports the hypothesis of FeO depletion over much of Mercury's surface, but also identifies specific regions richer in FeO and TiO_2 that has been excavated from depth by impacts [16]. Results from MESSENGER's neutron spectrometer during its third and final flyby [27], however, provide apparently contradictory results. They indicate that Mercury's surface may have abundant neutron-absorbing materials, of which the most likely are rich FeO and TiO_2). The contradictory data could potentially be reconciled by the presence of opaque phase such as ilmenite ($FeTiO_3$). Analysis of equilibrium crystallization [48] prohibits the coexistence of such iron-rich oxides with a $\lesssim 3$ wt.% FeO silicate, and suggests that magnesium-rich titanium oxides might be the cause of the signal. This also does not rule out production of ilmenite by non-equilibrium processes, and the extent to which space weathering and cosmogenic pollution is affecting the data is unknown.

I.5. Moment of Inertia

The principle moments of inertia of a planet can be determined from the trajectory of a nearby body such as a spacecraft. This has been done using the Mercury Laser Altimeter (MLA) during MESSENGER's fly-bys [53]. These principle moments of inertia allow for determination of the density distribution within the planet, and provide another potential constraint on the bulk mantle iron to silicate ratio. In addition, this data will place better constraints on the size of the core, which would better determine the overall iron to silicate ratio. The fly-by data does not have sufficient resolution for such a constraint, but this resolution should be greatly improved once MESSENGER is in orbit around Mercury.

TABLE I. **Physical properties of the terrestrial planets and their cores:** A comparison of the radii of the terrestrial planets and their cores, demonstrating Mercury’s anomalously large iron core. Planet dimensions and densities taken from de Pater and Lissauer 2001 [17]. Fe-Si ratios are calculated from the uncompressed density, assuming a pure Fe core and pure forsterite mantle. The solar Fe-Si ratio is calculated from tabulated spectroscopic values from Lodders 2003 [31]

	$R_{equatorial}$ (km)	r_{core} (km)	ρ_{avg} (gcm^{-3})	$\rho_{uncompressed}$ (gcm^{-3})	$\frac{M_{Fe}}{M_{silicate}}$	$\frac{N_{Fe}}{N_{Si}}$
Mercury	2440	1850	5.43	5.3	2.6	6.5
Venus	6042	3488	5.20	4.3	0.82	2.1
Earth	6378	3000	5.515	4.4	0.93	2.4
Mars	3390	1480	3.74	3.74	0.31	0.78
Solar	-	-	-	-	-	0.8128

TABLE II. **Motivating results of SPH simulations by Benz et. al. 2007:** The 7 out of 17 SPH simulations from Benz et. al. 2007 [6] that best recreate present day Mercury. All simulations used the same initial conditions listed below under ‘initial’. ‘cold’ and ‘hot’ refer to the initial thermal state of the planet which was varied for some simulations. The impact parameter b is the offset of the collision from an on axis collision at 0 in units of Radii of the target body. m_{imp}/m_{tar} is the ratio of the masses of the impactor and the target and M_f is the ratio of the final mass to the mass of present day Mercury.

$type$	b	m_{imp}/m_{tar}	v (km/s)	$\frac{M_{Fe}}{M_{silicate}}$	M_f
initial	—	—	—	.50	2.1
cold	.53	.167	28	.159	1.01
cold	0	.167	20	1.63	.92
cold	.6	.2	30	1.06	.94
cold	.5	.2	28	1.96	.86
hot	0	.2	19	1.48	1.01
hot	.46	.2	25.5	1.96	.87
hot	.5	.2	28	2.04	.85

II. PROPOSED SCENARIO

This work puts forward a new mechanism to explain how a planet could obtain both a large reduced iron core and a mantle depleted in oxidized iron, while still starting with a bulk planetary composition similar to that of the Earth. The early condensates in a large impact plume are magnesium-rich, leaving iron-rich vapor to be removed by solar wind. The reaccreting magnesium-rich condensates produce an iron-poor, lower-mass Mercurian mantle. This is by no means a unique solution to the problem of creating these two anomalous aspects of the planet; however, to our knowledge it would be the only such hypothesis that suggests both could result from the same formative event.

II.1. Initial Conditions and ‘Parcel’ Method

As a starting point, we consider impacts of similar intensity to the successful cases from Benz 2007 [6], in which their SPH simulations resulted in sufficient loss of material to reach bulk densities similar to present-day Mercury. These impacts, with an approximately Mars-sized target body and of an impactor with ~ 0.2 times that mass, require a high relative velocity of $\sim 20\text{--}30$ km/s, at which gravitational acceleration between the two bodies is negligible. Assuming that a significant fraction of the initial energy budget of the collision, on the order of 10^{31} J, is converted into thermal energy, it can be concluded that a significant portion of the ejected material would be completely vaporized. This conclusion is also supported using semi-analytic models of the impact compression and release (see Section III). The most energetic portions of the ejected vapor would largely escape Mercury’s sphere of influence following the impact, as shown by SPH simulations [4–6].

We assume that the rate of expansion of the plume is fast enough such that the thermodynamic properties of any particular region can be tracked without detailed knowledge of any other region of the plume. For this reason, the majority of our analysis is concerned with tracking the evolution of a single ‘parcel’ of ejected material from an initial vapor dominated state through the process of condensation. These parcels would expand with time such that per volume parameters would decrease by a simple function of distance traveled. This method avoids the complexities associated with a full three dimensional model of a vapor plume, while allowing us to evaluate conditions that determine the evolution of the

plume material on small length scales. The method presented here alone cannot yield predictions for changes in bulk composition of the planet, but should be able to predict the state of material in a particular portion of the plume. This method could then be coupled with a hydrodynamic simulation of the initial decompression stages of a plume to predict the amount of material which is ejected under the range of conditions where iron-magnesium differentiation could occur.

II.2. Homogeneous Condensation

As a completely vaporized parcel of silicate material cools, the first phases to condense are expected to be minor refractory phases including Al_2O_3 , $CaTiO_3$ and a variety of aluminosilicate phases [31]. Because the first condensation occurs in a state in which there are no existing nucleation sites, there will be an initial step of homogeneous nucleation of such phases. Homogeneous nucleation refers to the formation of condensed particles in a supercooled vapor. It's rate is limited by the energy barrier that must be overcome to increase the surface area of a very small, condensed particle. This step will lead to the formation of a number of condensation centers that would not be significantly increased during subsequent condensation steps as the more abundant silicate phases would condense onto the surfaces of the nucleation centers, increasing the particle size rather than the number. This nucleation step, therefore, is essential in determining the evolution of the ejecta plume. There are many discussions of homogeneous nucleation theory in the literature [35, 46, 51], but few that deal with systems similar to the one considered here, where the nucleation is limited by minor elemental components.

In a qualitative sense, consideration of this step should lead to fewer nucleation sites and thus a larger final particle size than previously predicted [4, 6]. In the calculations presented here, we assume a final particle radius on the order of 1 cm, which is an order of magnitude higher than results from [4] that utilize the homogenous nucleation theory of Raizer 1960 [46] on an assumed system of pure forsterite. In addition to affecting the efficiency of removal by Poynting-Robertson drag, this change in particle density affects the interaction between the condensed droplets and the vapor. Smaller, more numerous condensed particles would lead to less spatial separation between initially co-moving vapor and the droplets (See Appendix A) and also limit the extent of expansion under which equilibrium condensation can occur

(see Appendix B).

The condensation of such high temperature oxide and silicate phases prior to the more abundant magnesium rich silicates is expected based on extensive thermodynamic modeling of condensation from nebular gas. Additional work is necessary to verify that this is the case for the much higher partial pressures that would be expected in the vapor plume. The presence of unvaporized grains in the ejecta cloud might have a similar effect, but their density would be controlled by a different mechanism.

II.3. Equilibrium Condensation

The focus of our calculations is the behavior of a parcel of material in the regime in which the major silicate phases condense in equilibrium. The evolution of a parcel in this regime is driven by the high specific heat of vaporization of the phase. Both the magnesium-rich and iron-rich silicates have a similar heat capacity, but the magnesium-rich phases are more refractory and would condense first at higher temperatures [41]. As a result, the dominant magnesium-rich phases buffer the temperature resulting in a delayed (with respect to the extent of expansion) start to the condensation of more volatile phases.

This delay in condensation might lead to a depletion of FeO by two means. Equilibrium condensation can only occur over a limited range of conditions, because it requires a sufficient frequency of interactions between gas molecules and condensate droplets. For this reason, a criterion for the extent of expansion over which equilibrium condensation occurs can be derived by comparing the average time for a vapor molecule to interact with a droplet to a characteristic timescale for expansion. We use the doubling time of the radius of the vapor plume as this characteristic timescale (see Appendix B). As a result, some proportion of material, enriched in iron due to condensation of magnesium-rich silicates will not condense. A significant amount of the condensed ejecta may then reaccrete, while the iron enriched vapor will be unable to accrete quickly enough.

A second means for FeO depletion could also occur as a result of spatial separation between the condensate and the vapor that is accelerated by a pressure gradient (See Appendix A). Although it is unclear how to evaluate the significance of this second mechanism, its efficiency should depend on the size of the condensate droplets.

II.4. Removal Versus Reaccretion of Ejected Material

Material that has enough kinetic energy to escape Mercury’s gravitational sphere of influence would expand into a torus of material around the sun. Incomplete condensation would lead to a roughly bimodal size distribution in material present at this orbital radius for some time after the impact. Such a bimodal , consisting of SiO gas and quenched silicate droplets, has in one case been identified around another star, and is interpreted to be the result of such a giant impact [30].

Material that remains in the vapor phase will be removed on a relatively short timescale due to interaction with solar wind. For a discussion of these timescales see Appendix C. The material partitioned into the vapor will therefore be reaccumulated in negligible quantities. The fate of condensed material is less certain. At the average particle radius of 1 cm assumed in this paper, the strongest removal process is expected to be the Poynting-Robertson drag, which causes a loss of angular momentum and thus a decreasing orbital radius. This removal process occurs on a similar timescale as reaccretion of the material [6]. This timescale, however, would rely to a great extent on the specifics of nucleation, which to date has not been completely addressed.

Material that is not removed from Mercury-crossing orbits during sufficiently short timescales would be reaccreted onto the planet. This influence the planet’s bulk composition. If this reaccreted material is sufficiently FeO-depleted and has a mass comparable to that of Mercury’s mantle, then it would lead to noticeable FeO depletion in mantle silicates.

II.5. ‘Road Map’

This thesis is divided up into three sections: one focused on related work motivating the differentiation mechanism suggested here, one focused on the of a simple model of the mechanism, and another discussing the potential role of this mechanism in planet formation. Section III utilizes existing semi-analytic models for the distribution of energy during the compression of an impact to verify the assumption that vapor production would be significant for this scale of impact. Section IV presents the results of thermodynamic models coupling a simple chemical model of a silicate vapor plume to an isentropic expansion into a vacuum to evaluate the extent to which the latent heat of vaporization drives the expansion of the

vapor plume. Finally, Section V is devoted to the discussion of the results and potential effects of this mechanism, as well as criteria which might be used to identify it against the other popular models for Mercury’s formation. We finally provide appendices for additional calculations carried out in support of methods in the three main sections.

III. VAPOR PRODUCTION

Hyper-velocity impacts irreversibly compress material to supercritical states. Following these extreme conditions the material will release to produce vapor, liquid, and solids in different regions of the impactor and target, depending on the intensity of the shock. Compositional fractionation is most likely to occur in the vapor phase, so the mass of vapor following impact is a critical parameter for these models. The work in this section therefore validates necessary assumptions of the scenario presented in Section II. These calculations also place upper limits on the efficiency of differentiation resulting from a given intensity of impact.

III.1. Shock Compression

The equations governing material in a shocked state, called the Hugoniot equations, are conventionally written

$$\rho(U - u_p) = \rho_0 U \quad (1)$$

$$P - P_0 = \rho_0 u_p U \quad (2)$$

$$E - E_0 = \frac{1}{2} (P + P_0) (V_0 - V) \quad (3)$$

where P is pressure, ρ is density, E is the specific internal energy, $V = \rho^{-1}$ is the specific volume, U is the shockwave velocity, and u_p is the particle velocity. The subscript “0” refers to the unshocked values of the corresponding quantity. Every material has a particular Hugoniot curve that describes its state for a given intensity of shock. The shock compression is thermodynamically irreversible, and any point along the Hugoniot is a peak compression in a given material which undergoes a shockwave of a particular intensity. After the initial shock the material releases via an adiabatic path, therefore the location of the shock upon the Hugoniot determines the state of the released material [37]. Figure 1 shows a calculated

M-ANEOS [38] Hugoniot and the boundary of a two-phase (liquid-vapor) region for dunite in pressure-specific volume space. Upon determining the correct adiabat, the lever rule can be used to estimate the proportions of liquid and vapor in the portion of phase space in which they coexist.

III.2. Semi-Analytic Methods

Fully addressing the complexity of vapor production by an off-axis collision requires use of three-dimensional hydrocode [44]. However, there have been a variety of attempts [14] [45] [55] [56] to create semi-analytical models of on-axis collisions to estimate energy distribution as well as melt and vapor production. These semi-analytical models use simplified geometries to capture the qualitative features of energy distribution determined by two-dimensional hydrocodes [45]. These simulations indicate that the shockwave created by the impactor leads to a relatively constant, near-field pressure region [1], often referred to as the isobaric core. In order to estimate the fraction of vapor produced by the impact, we first use an analytic solution for an idealized planar impact to calculate the pressure of the isobaric core. We then use a scaling law to estimate the size of the isobaric core. We then extrapolate the pressure for material outside the isobaric core and use material Hugoniots to determine the release adiabats, which determine the final state of the released material.

The far-field regions for both the shock pressure [14] and particle velocity [45] have been shown to be well described by a decay law:

$$P(d) = P_{ic} \left(\frac{r_{ic}}{r} \right)^n \quad (4)$$

where r_{ic} and P_{ic} are the radius and pressure within the isobaric core, r is the distance of the shockwave from the center of the isobaric core, and n is a fit exponent whose value depends on the impact velocity [45].

Tonks and Melosh, 1993 [56] present two end-member models in which a spherical isobaric core is assumed to occur centered on or tangent to the surface, with its radius proportional to the kinetic energy of the impactor. However, increased resolution 2-D hydrocode simulations [45] indicate that the depth of the isobaric core is itself a function of the impact velocity and, in fact, scales more rapidly than the radius. For this reason, we are utilizing a generalization of the models presented by Tonks and Melosh, in which the isobaric core is treated as a

buried sphere with a radius and depth determined by the impact velocity. For each of these parameters we use relationships of the form:

$$A = a + b \cdot \log_{10}(v_i) \quad (5)$$

with the parameters presented in Pierazzo, 1997 [45] for dunite. Here a and b are fit constants, while A is any of the three parameters of interest: n , $\log_{10}\left(\frac{r_{ic}}{r_{proj}}\right)$ or $\log_{10}\left(\frac{r_{ic}}{d_{ic}}\right)$, where r_{proj} is the radius of the projectile and d_{ic} is the depth of the isobaric core. We then assume that pressure decreases in spherically symmetric fashion using Equation 4.

III.3. Impedance Matching Technique

The pressure within the isobaric core was calculated through the standard impedance matching technique [37], which approximates impact as a collision of two infinite slabs. Equations 1-3 are applied to the two shocks propagating through either slab, and the requirement that the particle velocity for material in both slabs be equivalent leads to the equality $u_t = v_i - u_p$, where u_t and u_p are the particle velocities for the target and projectile slabs, and v_i is the impact velocity. This relationship allows for a graphical determination of the pressure. We find the intersection in P - u space of the target Hugoniot with the projectile Hugoniot inverted and translated by v_i . The calculated isobaric pressure thus increases with the chosen value for v_i , as in Figure 2. Our values for the isobaric core pressure use the M-ANEOS dunite Hugoniot for both the target and projectile. We consider impact velocities in a similar range (20-35 km/s) to that considered by Benz et. al. 2007 [6]. For our assumptions of identical target and projectile Hugoniots yield a plot symmetric about the intersection at $u_t = u_p = \frac{1}{2}v_i$. This method yields isobaric pressures ranging from 650 to 1650 GPa.

Each peak pressure on the Hugoniot corresponds to a unique specific entropy of the shocked material. While the compression of the material in the shockwave is a thermodynamically irreversible process, the releasing of the material can be well approximated by an adiabatic expansion from the initial compressed state on the Hugoniot [37]. The intersection of this adiabat with the boundary of the two-phase regime can then be used to estimate the fraction of material that is vaporized. This is most easily visualized in pressure-entropy space (Figure 3), in which each adiabat is represented by a constant value in entropy. The

entire tested range in impact velocities is within the two-phase regime and all lead to a vapor fraction of $>50\%$ for material released from the isobaric core. For 20 km/s the isobaric core release to a vapor fraction of slightly over 50%, while for 35 km/s the vapor fraction nears 100%.

III.4. Experiment Versus Modelling

All of the methods presented involve inherent assumptions about the materials, and remain firmly in the realm of analytic chemical models due to the inaccessibility of the desired region of phase space with current experimental methods. All of the scaling relationships developed for the semi-analytic models [14] [45] [55] [56], as well as SPH simulations [4–6] rely on predictions from codes like M-ANEOS to base their calculations. High-pressure shock experiments have only in the last couple of years reached conditions under which vaporization of silicate materials has been detected. These experiments indicate that the analytic chemical models are incomplete; laser-induced shock experiments on SiO_2 [26] have been found to be reasonably compatible with the M-ANEOS equations for liquid-solid phase boundaries, but indicate that the code significantly underestimates the specific entropy of material on Hugoniot. This corresponds to SiO_2 vaporization occurring more readily than previously predicted. A similar trend may exist for Mg_2SiO_4 and other silicates. This introduces an unavoidable level of uncertainty, even for the simplest of impact geometries. If vaporization is underestimated by current techniques, then the efficiency of the proposed mechanisms would be greater.

III.5. Vapor Production Results

The vapor plume is ejected on relatively short timescales, and the vaporization fraction is likely to be intimately connected to the dynamics of the material sourced from any particular location in the target. For this reason, we present the data in terms of ranges of vapor fraction at distances from the center of the isobaric core. It should be noted that for these simple models we do not attempt to take into account any interaction with an iron core, which would exhibit different shocked and released behavior than the silicate mantle. Additional work on the evolution of two phase flows in the ejecta plume is necessary to determine a

better criterion for how material of a given vaporization fraction will evolve.

The important result is that the impact intensities considered in this study cause a significant portion of the target’s mantle to be shocked and subsequently released to states dominated by silicate vapor phase. This is a necessary prerequisite for the fractionation of silicates by the process introduced in Section II, as the identification of any compositional anomaly involving bulk mantle composition would require that the process act on a volume of material corresponding a large percentage of the total planet.

Figures 4 and 5 show the size of a sphere representing the location where shocked material would be released to incipient vaporization or 50% vaporization as well as the isobaric core for two different impact parameters, for impactors with a mass ratio of .2 and impact velocities of 20 and 30 km/s. To avoid the ambiguity inherent in choosing a pressure at which to use the lever rule, we choose “50%” to be the shocked state corresponding to material releasing to the peak of the two phase region. This makes the calculated sphere slightly larger, with the discrepancy growing as pressure decreases due to the asymmetry of the curve in P-S space.

FIG. 1. Olivine Hugoniot and liquid-vapor phase boundary: The M-ANEOS Hugoniot plotted in pressure-specific volume space with the phase boundary for the two-phase (liquid and vapor) region. After being being compressed to a point along the Hugoniot by the shockwave, material releases adiabatically until reaching the boundary. The point along this boundary then determines the vapor fraction of the released materials

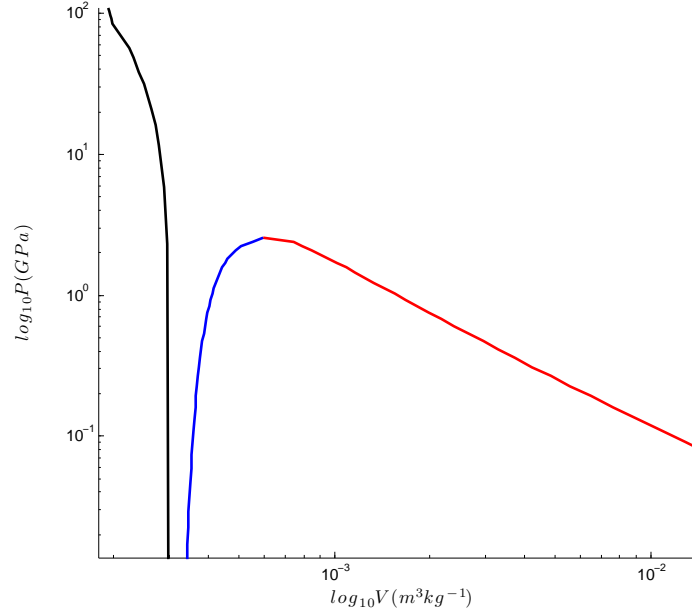


FIG. 2. Impedance matching technique with olivine Hugoniot for various impact velocities: Estimates of isobaric core pressure using the impedance matching technique, utilizing the solution for two colliding infinite planes. The M-ANEOS dunite hugoniot is used and is translated by a range of velocities (20, 25, 30, 35 km/s) corresponding to the relative velocity between the bodies at impact.

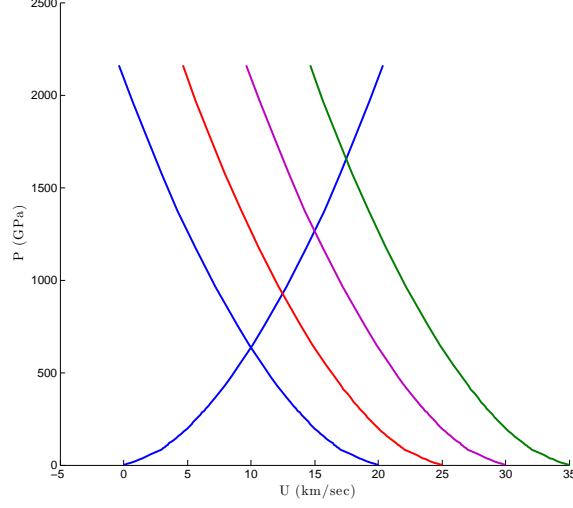


FIG. 3. Decompression adiabats and liquid-vapor phase boundaries: M-ANEOS liquid-vapor phase boundaries and the adiabats corresponding to the release from the shocked state within the isobaric core for each of the impact velocities in Figure 2 in pressure-specific entropy space. For a given pressure the lever rule can then be used to estimate the vapor fraction at a given pressure.

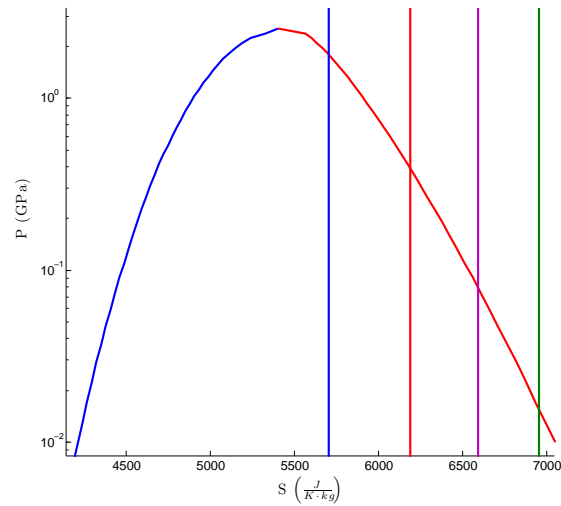


FIG. 4. Effect of impactor velocity on vapor productions: Cross-section view of isobaric core and vapor-fraction regimes for an impactor with .2 times the target's mass and a relative velocity of 20 km/s and 30 km/s. The red circle denotes the size of the isobaric core. The orange circle denotes the size of a sphere releasing to a 50% vapor fraction. The yellow circle denotes the extent of a sphere of incipient melting.

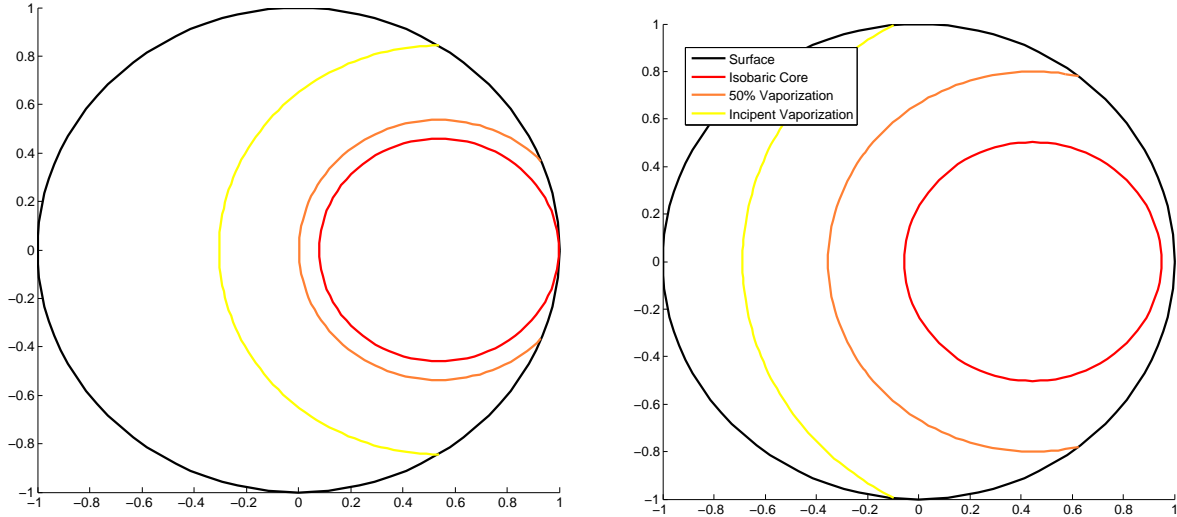


FIG. 5. Effect of impactor mass on vapor productions: Cross-section view of isobaric core and vapor-fraction regimes for an impactor with .1 and .2 times the target's both with a relative velocity and 30 km/s. Colors denote the same meaning as in Figure 4.

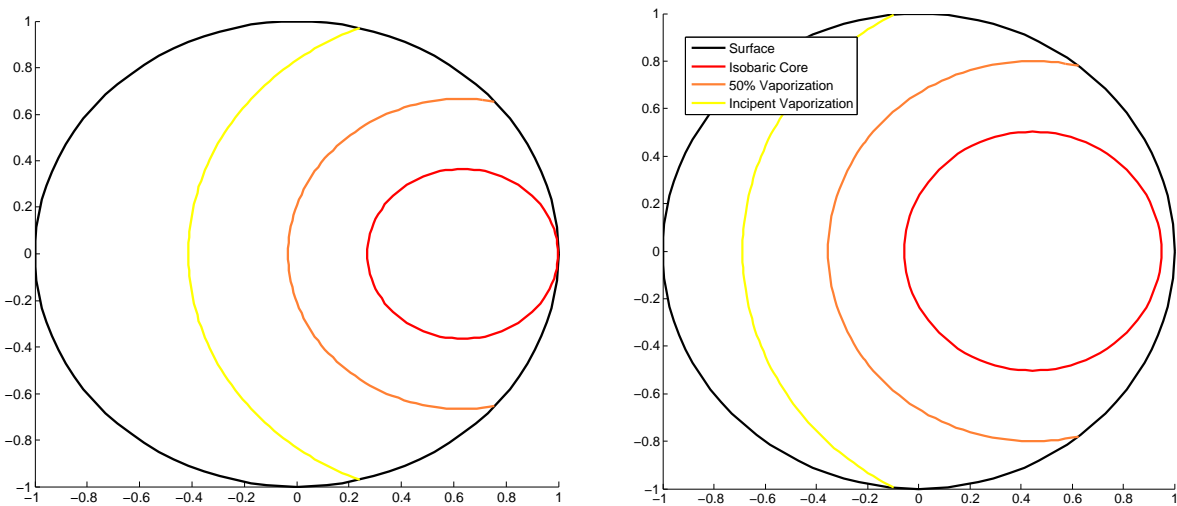


TABLE III. **Estimates for vapor production using the semi-analytic methods I:** Calculation of vapor fraction ranges using the semi-analytic method for $M_{imp}/M_{tar} = 0.1$. All radii are in units of target radii and all volumes are in units of target volume.

Impactor Velocity (km/s)	20	25	30	35
Peak Pressure (GPa)	630	925	1265	1654
Entropy (J/kg*K)	5702	6189	6594	6956
Calculated Radii:				
depth	0.366	0.405	0.439	0.471
isobaric radius	0.365	0.383	0.399	0.412
half (2 phase peak) (495 Gpa)	0.426	0.541	0.635	0.716
incipient (245 Gpa)	0.669	0.798	0.9	0.986
fractional volumes:				
isobaric core	0.0485	0.0562	0.0636	0.0703
half vap	0.0756	0.146	0.225	0.308
incipient vap	0.231	0.361	0.483	0.598

TABLE IV. **Estimates for vapor production using the semi-analytic methods II:** Calculation of vapor fraction ranges using the semi-analytic method for $M_{imp}/M_{tar} = 0.2$. All radii are in units of target radii and all volumes are in units of target volume.

Impactor Velocity (km/s)	20	25	30	35
Peak Pressure (GPa)	630	925	1265	1654
Entropy (J/kg*K)	5702	6189	6594	6956
Calculated Radii:				
depth	0.461	0.51	0.554	0.593
isobaric radius	0.459	0.483	0.502	0.52
half (2 phase peak) (495 Gpa)	0.537	0.681	0.8	0.901
incipient (245 Gpa)	0.841	1.006	1.13	1.24
fractional volumes:				
isobaric core	0.0971	0.112	0.127	0.140
half vap	0.150	0.287	0.433	0.578
incipient vap	0.435	0.6478	0.818	0.941

IV. MODELING THE EXPANDING VAPOR PLUME

Once the ejecta has been released from its compressed state, the regimes dominated by vapor will undergo an evolution similar to adiabatic expansion into a vacuum. During this phase such vapor-rich plumes will ‘outrun’ those containing a more significant fraction of liquid or solids, as kinetic energy from the gas goes into accelerating the more massive particles. We therefore model the simple case of a spherical vapor plume expanding into a vacuum, while the vapor is condensing into liquid droplets. Analytic solutions for the sudden isentropic expansion of a spherical vapor cloud are presented in Zel’dovich and Raizer 1966 [59], and discussion of single component nucleation and condensation under such conditions is presented in Raizer 1960 [46]. Here we present simple numerical models coupling this symmetric isentropic expansion for a multicomponent silicate vapor condensing into three liquid components. The handling of the thermochemical side of the calculations is similar to that done by Pahlevan and Stevenson 2007 [42] in their model of isotope equilibration in a gaseous disk following the moon forming impact.

IV.1. Thermodynamic Model

We assume a highly simplified chemical model for evaluating the evolution of the expanding vapor plume, including only four elements (oxygen, silicon, magnesium and iron) expected to be most abundant in a vaporized sample of a terrestrial mantle. Using the Earth’s bulk mantle values from Hart and Zindler [22]. The oxide weight percents are 46.3 for SiO_2 , 38.4 for MgO and 7.7 for FeO . This corresponds to a Fe # ~ 0.1 , which we use in our model. The next most common are Al_2O_3 , CaO with a weight percent 3.96 and 3.2 respectively. Neither would be expected to go into a magnesium rich silicate phase, and both would have an energetic effect at least an order of magnitude smaller than the dominant magnesium-rich phase.

With these four elements we expect the important vapor species, $O_{(v)}$, $O_{2(v)}$, $Si_{(v)}$, $SiO_{(v)}$, $SiO_{2(v)}$, $Mg_{(v)}$, $MgO_{(v)}$, $Fe_{(v)}$ and $FeO_{(v)}$, to exist in varying proportions governed by their thermodynamic properties. At the temperatures at which condensation would occur, one can verify that thermal ionization should not play an important role using the Saha equation.

We choose representative condensed phases that likely behave similarly to the true bulk

silicate composition: Forsterite ($Mg_2SiO_{4(l)}$), Fayalite ($Fe_2SiO_{4(l)}$) and reduced iron ($Fe_{(l)}$). In this first model we treat the condensation of our two silicate phases separately, when in reality they would condense as a solution. Nonetheless, the FeO proportion in high temperature olivine should be very low [43]. Thus, we assume this to be a reasonable first approximation for following the energetics of the vapor plume evolution.

With these components, there are a total of eight reactions which would govern the proportion of the components into a liquid and vapor phase at equilibrium. Thermodynamic data for all of these phases [13, 19, 42] was used to determine a temperature relationship for the equilibrium constants of the eight reactions. The thermodynamic data was fit to an assumed relationship of

$$\ln K = A - \frac{B}{T} \quad (6)$$

of which constants A and B are tabulated for all reactions in Table V and K is the equilibrium constant.

IV.2. Computational Methods

The behavior of the expanding plume depends upon the number of moles of vapor per parcel, which is decreased from that of a monatomic gas by the presence of polyatomic vapor phases and condensed phases. So we define

$$x_{gas} = \sum_i x_i \quad (7)$$

where x_i is the moles of vapor phase ‘i’ in a parcel with one mole of atoms. Using x_{gas} we denote the molar volume of the gas as

$$\nu_{gas} = x_{gas}\nu \quad (8)$$

where ν is the molar volume of total atoms. For a parcel with one mole of atoms at very high temperatures, when most of the parcel consists of a monatomic vapor, x_{gas} will be approximately unity. For every reaction considered, there is a relationship defining the equilibrium constant in terms of the pressure and composition. For example the reaction $MgO_{(v)} \rightleftharpoons Mg_{(v)} + \frac{1}{2}O_{2(v)}$ has the following expression for its equilibrium constant

$$K = \left(\frac{P}{x_{gas}} \right)^{\frac{1}{2}} \frac{x_{mg} x_{O_2}^{\frac{1}{2}}}{x_{MgO}} \quad (9)$$

where P is the total pressure and K is the equilibrium constant. Making use of logarithmic derivatives, this leads the differential expression

$$\frac{1}{2} \left(\frac{\partial P}{P} - \frac{\partial x_{gas}}{x_{gas}} \right) + \frac{\partial x_{Mg}}{x_{Mg}} + \frac{1}{2} \frac{\partial x_{O_2}}{x_{O_2}} - \frac{\partial x_{MgO}}{x_{MgO}} = \frac{B}{T} \left(\frac{\partial T}{T} \right) \quad (10)$$

where B is the constant from the thermodynamic relationship $\ln K = A + B/T$ for the particular reaction. It should be noted that Equation 10 can also be written in terms of the partial pressures.

We assume an ideal atomic gas such that

$$P\nu_{gas} = RT \quad (11)$$

$$\frac{\partial P}{P} + \frac{\partial \nu}{\nu} + \frac{\partial x_{gas}}{x_{gas}} = \frac{\partial T}{T} \quad (12)$$

and that the expansion occurs sufficiently rapidly and with negligible liquid-vapor separation so that the process is isentropic. We assert that this is a reasonable assumption as the plume would be optically thick during the timescales of interest, and would therefore not lose significant energy due to radiation. From the first law of thermodynamics,

$$T\partial S = \partial u + P\partial \nu_{gas} = 0 \quad (13)$$

for an isentropic process. S is the entropy and u is the internal energy. The change in internal energy must include terms for the cooling of the vapor-liquid mixture as well as the energy release from the process of condensation. We use the relationship

$$\partial u = C\partial T - \sum_j U_j \partial x_j \quad (14)$$

where C is a function of the compositions, x_i and x_j , and their respective specific heat capacities. U_j is the specific heat of vaporization for each condensed phase j . Using the previous relationship we can write the work due to expansion as

$$P\partial \nu_{gas} = \frac{RT\partial (x_{gas}\nu)}{x_{gas}\nu} = RT \left(\frac{\partial \nu}{\nu} + \frac{\partial x_{gas}}{x_{gas}} \right) \quad (15)$$

which yields the following expression of isentropy with $\bar{C} = \frac{C}{R}$ and $\bar{U} = \frac{U}{R}$.

$$\bar{C}(x_i, x_j) \left(\frac{\partial T}{T} \right) + \frac{\partial \nu}{\nu} + \frac{\partial x_{gas}}{x_{gas}} = \sum_j \bar{U}_j \partial x_j \quad (16)$$

This expression is similar to that used in the simpler models [46, 59]. Our method implicitly assumes a starting entropy which is held constant throughout the calculation. Assuming a different starting entropy leads to a different unique thermodynamic path.

We now require four more equations to match the variables considered. This is satisfied by considering the mass balance of the four considered elements.

$$\partial x_{MgO} + \partial x_{Mg} + 2\partial x_{fo} = 0 \quad (17)$$

$$\partial x_{FeO} + \partial x_{Fe(v)} + 2\partial x_{fa} + \partial x_{Fe(l)} = 0 \quad (18)$$

$$\partial x_{SiO_2} + \partial x_{SiO} + \partial x_{Si} + \partial x_{fo} + \partial x_{fa} = 0 \quad (19)$$

$$\begin{aligned} 7\partial x_{fo} + 7\partial x_{fa} + 3\partial x_{SiO_2} + 2\partial x_{SiO} + \partial x_{Si} + 2\partial x_{MgO} + \partial Mg... \\ + 2\partial x_{FeO} + \partial x_{Fe(v)} + \partial x_{Fe(l)} + 2\partial x_{O_2} + \partial x_O = 0 \end{aligned} \quad (20)$$

The first three equations represent a mass balance between species containing magnesium, iron and silicon respectively. The final equation represents a mass balance of total molecules. An equation for the mass balance of oxygen containing species would be equivalent.

We use a step-wise approach in our calculations, in which we define a criterion for which a particular condensed phase is considered to be present in the system. For this we use the criterion put forward by Grossman 1972 [21], in which condensation begins where the value of the equilibrium constant calculated from Equation 9 with the calculated partial pressures involved is equivalent to the equilibrium constant found from the expression using the relevant coefficients from Table V. At this criterion, the equation in the form of Equation 10, describing the equilibrium condensation of that phase, is added to the set of similar equations involving reactions among the vapor phases. To determine the initial proportions of gaseous phases, we use a rapidly-converging method of minimizing the remainder of the non-differential equations [21] for the equilibrium reactions between vapor phases, the ideal behavior of gas, and mass balance. We then iteratively solve the differential equations for all reactions along with Equations 12, 16, and 17-20 with a specified $\frac{\partial T}{T}$. Repeatedly applying this method to a region of phase space allows us to produce a ‘phase diagram’, Figure 6,

showing the conditions at which each considered phase would be included. Each phase of simulated condensation is run until it reaches a region of phase space in which another phase is stable.

Because the equations derived above depend on the assumption of equilibrium condensation, they will only be valid over a range of conditions. Once the gas becomes rarified to the point where the collision of vapor molecules with the condensed droplets becomes the limiting factor, the rate of condensation would drop significantly and whatever portion of vapor remaining we assume has failed to condense. By comparing the timescales of molecular collisions to the timescale of expansion, we derive a criterion for the extent of expansion before equilibrium condensation ceases (see Appendix B). We find that this cutoff criterion occurs when the plume reaches a molar volume on the order of $10^4 \frac{m^3}{mol}$. The relevant parameters in our simulations at this cutoff are thus taken to as estimates for the escaping material for any particular starting entropy.

IV.3. Results

The results of our calculations demonstrate that, for reasonable assumptions about the starting entropy of a parcel, the condensation of forsterite significantly delays or prevents condensation of fayalite. Figure 7 shows the evolutionary pathway of one such parcel, assuming equilibrium reactions exist throughout the expansion. There are three evident steps in this condensation. The first, represented by a steep slope on the $\log_{10} V$ - T plot, is the adiabatic expansion of vapor before condensation. This is followed by a step in which the majority of the forsterite condenses out, significantly increasing the extent of expansion per unit change in temperature compared to adiabatic expansion. Finally, fayalite condenses out in the third step in which. This behavior is seen for all of the assumed starting conditions, when equilibrium conditions are assumed to persist until 100% condensation. For all considered starting entropies, condensation of reduced iron did not begin before the equilibrium criterion was reached, and indeed did not occur in significant amounts even when the calculation was continued beyond reasonable assumptions of equilibrium.

Figure 8 shows the fraction of magnesium condensed as a function of the extent of expansion for the same initial conditions that produced the thermodynamic path in Figure 7. The assumption of local equilibrium is only reasonable to a molar volume of $\sim 10^4 \frac{m^3}{mol}$, at which

point escaping material is assumed to retain its partitioning between the liquid and vapor phase. In this case, for example, the material consists of a condensate containing $\sim 57\%$ of the total magnesium.

Assuming a higher initial entropy corresponds to a lesser extent of condensation at the condensation criteria. Since any definition of total entropy would be arbitrary to distinguish relatively high or low entropy cases. To identify a range of conditions for which fractionation would occur, we instead choose a proxy parameter. We categorize our simulations by the molar volume at which forsterite condensation begins, based on our calculations using the equilibrium constant data presented in Table V. Figures 7 and 8 thus correspond roughly to incipient condensation at $\nu_{mol} = 10^0 \frac{m^3}{mol}$. Higher initial entropies correspond to higher molar volumes (or lower temperatures) of incipient condensation. Figure 9 shows the thermodynamic paths produced by parcels at opposite ends of the entropy range for which incomplete condensation would occur. Higher starting entropies correspond to a lesser extent of expansion.

Table VI shows final results for calculations over a range of assumed starting entropies, for which we denote using molar volume at which forsterite condensation begins as a proxy variable. This range, with incipient forsterite condensation occurring between 10^{-2} and $10^1 \frac{m^3}{mol}$, is the range in which our proposed processes might lead to efficient depletion of FeO. For significantly higher entropies, the extent of forsterite condensation would be negligible and therefore the majority of the mass would finish of an undifferentiated vapor. For significantly lower entropies most of the major silicate phases would condense, leaving the majority of the mass in an undifferentiated condensate. It is possible that spatial separation (see Appendix A) might still lead to a lesser extent of depletion even in lower entropy cases.

It is also desirable to obtain a comparison between the conditions presented in Table VI and conditions expected for the impacts considered in Section III. As a first approximation of the conditions expected within the impact plume, we consider the specific entropies of the vapor predicted by the M-ANEOS Hugoniot after releasing isobaric core material for a given impact velocity. Using the specific molar volume and temperature as a point on an adiabat, we extrapolate to the point where it crosses into the regime of forsterite condensation. Figure 10 shows the adiabats for the vapor produced for the impact velocities considered in Section III. These values overlap with the lower end of the entropy range identified by the plume expansion simulations, as incipient forsterite condensation along

these adiabats occurs between $10^{-2.9}$ and $10^{-1.0} \frac{m^3}{mol}$. This assumes that the vapor decouples from its initially coexisting liquid and maintains an adiabatic path throughout the entirety of expansion.

The other result which may be of interest in identifying the aftermath of such an impact around another star is the proportions of vapor phases predicted. Figure 11 shows the evolution of vapor species proportions for cases with incipient vaporization at 10^1 and $10^{-2} \frac{m^3}{mol}$. In both cases significant amounts of Mg , O_2 and SiO should be abundant, but the lower entropy case also yields higher levels of O and MgO .

TABLE V. **Thermodynamic parameters of modeled liquid and vapor phases:** Parameters for a fit of equilibrium constant for the considered reactions, in the form of Equation 6. The first three reactions represent the condensation of three different liquid phases, while the next five are reactions between vapor phases. or the sources, C,P refers to relationships derived from Chase et. al. 1998 [13] by Pahlevan and Stevenson 2007 [42]. C,F refers to relationship derived from Chase et. al. 1998 [13] and verified against Fegley 1987 [19].

Reaction	A	$B(K)$	Source
$Mg_2SiO_{4(l)} \rightleftharpoons 2MgO_{(v)} + SiO_{2(v)}$	58.9	227,000	C,P
$Fe_2SiO_{4(l)} \rightleftharpoons 2FeO_{(v)} + SiO_{2(v)}$	49.6	180,000	C,P
$Fe_{(l)} \rightleftharpoons Fe_{(v)}$	14.62	45,370	C,F
$SiO_{2(v)} \rightleftharpoons SiO_{(v)} + \frac{1}{2}O_{2(v)}$	9.21	23,700	C,P
$SiO_{(v)} \rightleftharpoons Si_{(v)} + \frac{1}{2}O_{2(v)}$	8.14	67,300	C,P
$MgO_{(v)} \rightleftharpoons Mg_{(v)} + \frac{1}{2}O_{2(v)}$	2.9	9,310	C,P
$FeO_{(v)} \rightleftharpoons Fe_{(v)} + \frac{1}{2}O_{2(v)}$	6.33	20,900	C,P
$O_{2(v)} \rightleftharpoons 2O_{(v)}$	16.1	61,200	C,P

TABLE VI. **Range of conditions for which Fe-Mg fractionation is predicted:** Calculated percent condensation for a range of starting entropies, denoted by the molar volume at which condensation of forsterite begins. Higher entropy parcels have a higher value for $V_{mol,0}$, because they would expand further before incipient condensation.

$V_{mol,0}$ at Incipient Vaporization	% Mg Condensed	% Fe Condensed	Fe Number
10^1	50	0	0
10^0	57	0	0
10^{-1}	85	0	0
10^{-2}	>99	30	.032

FIG. 6. **Conditions for incipient condensation for modeled liquid phases:** Temperature versus molar volume of incipient condensation for Mg_2SiO_4 (green), Fe_2SiO_4 (blue) and reduced Fe (red), creating a ‘phase diagram’ for the portion of phase space relevant to our problem.

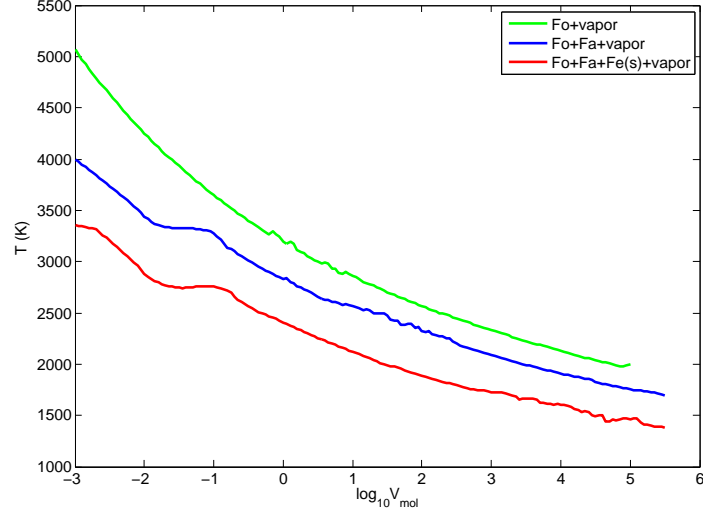


FIG. 7. **Thermodynamic path for representative vapor plume simulation:** This is the thermodynamic path (black) in T - $\log(v)$ space followed by a parcel during iterative calculations of the expanding mantle plume. For comparison, the condition of incipient condensation of forsterite (green) from Figure 6 is included. The initial entropy is such that the criterion for incipient condensation (see Figure 6) is satisfied at a molar volume of $\sim 1 \text{ m}^3/\text{mol}$

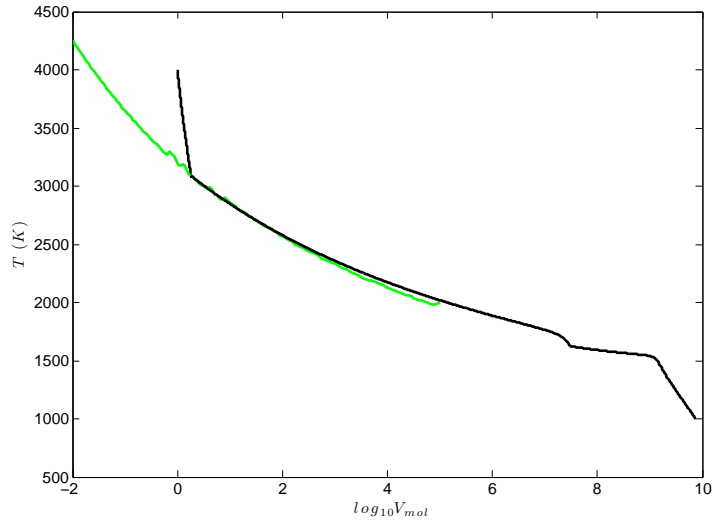


FIG. 8. **Fraction of Mg condensed for representative vapor plume simulation:** Fraction of Mg condensed as a function of the extent of expansion (molar volume) for an initial specific entropy corresponding to incipient forsterite condensation at $v_{mol} \sim 0 \text{ m}^3/\text{mol}$. These results correspond to the same simulation as in Figure 7. The condensation criterion assumes condensation halts at $v_{mol} \sim 10^4 \text{ m}^3/\text{mol}$

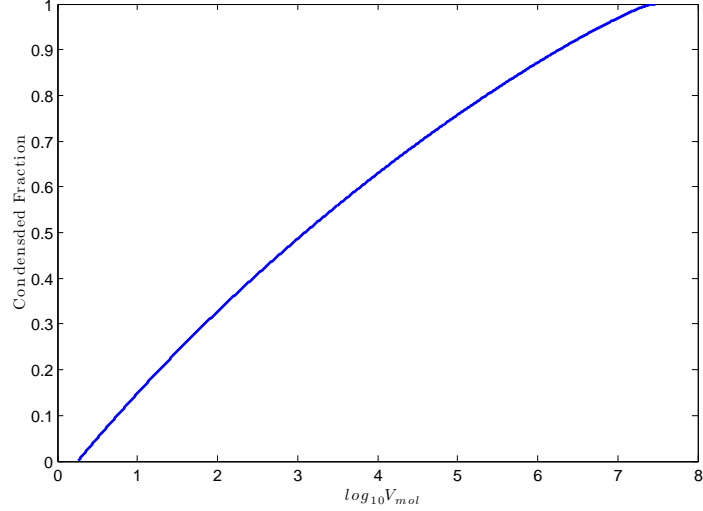


FIG. 9. **The effect of initial specific entropy on the thermodynamic path of expansion:** Thermodynamic path in T-log(V) space followed by parcels, for starting entropies corresponding to $\sim 10^{-1}$ (left) and $10^2 \text{ m}^3/\text{mol}$ (right). This corresponds to the range of conditions for which Fe-Mg fractionation is predicted to be significant. For comparison, the condition of incipient forsterite condensation is included.

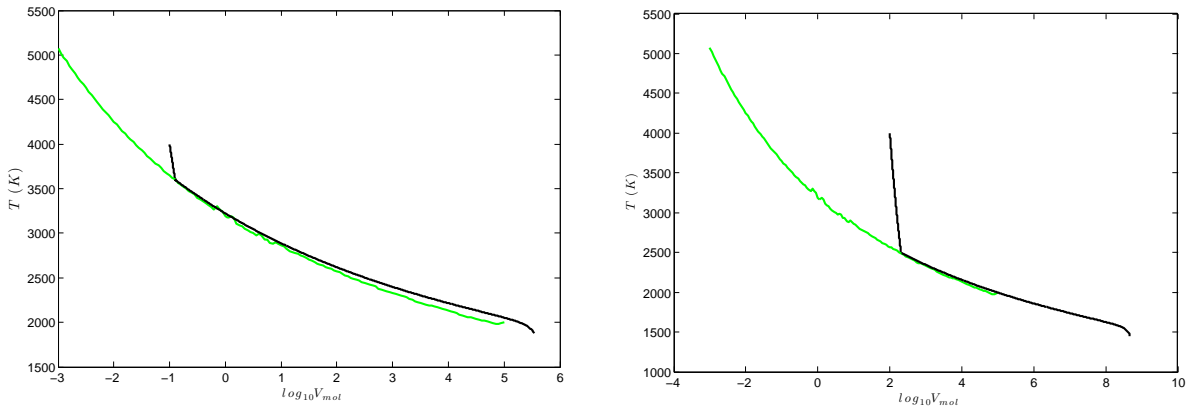


FIG. 10. Predicted conditions of incipient forsterite condensation for released vapor from isobaric cores: Extrapolated adiabats for expanding vapor produced by release from isobaric core conditions as determined from the M-ANEOS code. Adiabats (from left to right) represent conditions predicted for impact velocities of 20, 25, 30 and 35 km/s. The impedance matching technique from Section III was used to determine the molar volume and temperature of the vapor on the two-phase boundary, and to extrapolate the adiabatic expansion path assuming an adiabatic index for a diatomic gas.

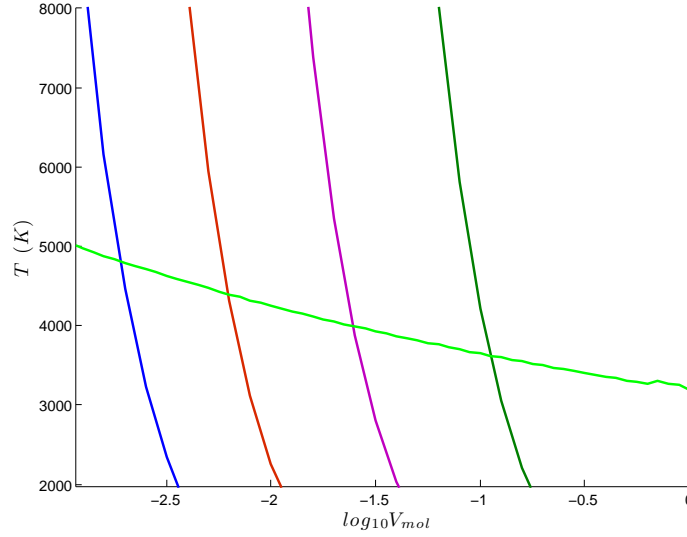
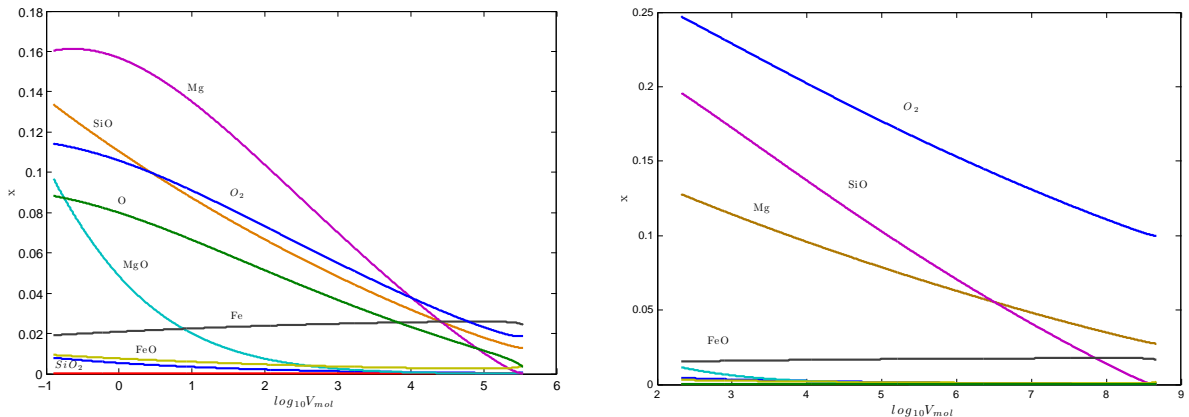


FIG. 11. The effect of initial specific entropy on the thermodynamic path of expansion: Abundance of considered vapor phases as a function of $\log(V)$ space followed by parcels for starting entropies corresponding to $\sim 10^{-1}$ and $10^2 \text{ m}^3/\text{mol}$. The abundances are normalized such that the total number of atoms is unity.



V. DISCUSSION

V.1. Motivation and Constraints from Modeled Vapor Production

The analytic and semi-analytic approximations presented in Section III present a reasonable first estimate for the energy distribution and vapor production for a near on-axis collision. The shape and depth of the isobaric cores indicates that, for impacts similar to our idealized case in geometry and magnitude, the pre-impact compositional profile of the mantle is unlikely to play a large role in the evolution of the plume. The regions of significant vaporization extend deep into the mantle, so a similar volume of material from the deep mantle will become vaporized as from the shallow mantle. Assuming that the evolution of different portions of the plume is controlled by the intensity of the shock and the vapor fraction produced by unloading, then the fairly uniform distribution of energy through the silicate mantle will result in similar evolution of material derived from all depths in the silicate mantle. As a result, preferential loss of elements enriched in the crust and upper mantle by magma ocean crystallization and subsequent gravitationally driven overturn [7] prior to an impact are unlikely to be the primary cause of compositional changes resulting from a near on-axis impact.

If a near on-axis giant impact is to be implicated as the progenitor of compositional differences in the silicate portions of terrestrial planets, a differentiation mechanism is required in which differentiation can occur from a more or less homogeneous target material. The mechanism explored in this paper fits this criterion, as it arises from thermodynamic properties of the mixture of silicate materials similar to that expected in terrestrial mantles. Since SPH simulations suggest that high angle (approaching on-axis) collisions are more efficient at increasing a planet's relative core size [4, 6], this corresponds to the more likely situation in an impact that significantly alters the ratio of reduced iron to silicates.

The results of Section III not only suggest the requirement of a new differentiation mechanism for the giant impact hypothesis, but also constrain the maximum efficiency of such a differentiation process. There is an inherent asymmetry in the geometry of a giant impact because energy is preferentially partitioned into the side of the target on which the impact occurs. The other side is largely shielded from the effects of the impact as the shockwave amplitude decays (see Figures 4 and 5). This means that, with the exception of impacts

intense enough to disrupt or nearly disrupt the target body, there is a sizable reservoir of mostly unaltered silicate material that is retained as a component of the post-impact silicate mantle. If this reservoir of material unaffected by the impact is significantly larger than the portion on which the differentiation acts, then the amount of differentiation would be so small as to cause only an indistinguishable change in bulk mantle composition.

The mechanism suggested here relies on the vaporization of material by the impact, so a prerequisite for the significance of said process is that the amount of vaporization be significant in proportion to the unaltered reservoir. Exactly what constitutes “significant vaporization” remains an open question. If we take it to be material for which the vapor fraction is 50% or higher, for instance, Tables III and IV show this corresponds to a volume fraction of the planet ranging from $\sim 10\text{-}60\%$ for increasing intensity of impact. If the differentiation were to act on 50% of the silicate mantle, then for the most extreme scenario an element could not be depleted by more than

$$\frac{\Delta f}{f} \sim \left[\frac{.5f}{1 - .5f} \right] \left(\frac{1}{f} \right) \cdot 100\% \quad (21)$$

or enriched by more than

$$\frac{\Delta f}{f} \sim \left[\frac{f}{.5(1 + f)} \right] \left(\frac{1}{f} \right) \cdot 100\%. \quad (22)$$

where f is the initial mole fraction of the element in question. Note that for this simple estimate ‘.5’ can be replaced with any fraction of the mantle involved on which the mechanism acts, and that for $f \ll 1$ these changes correspond to 50% and 200% respectively. Thus our results, indicate that a single impact event could lead to measurable, yet limited changes in composition.

We cannot discount the role of other sources of preferential element loss in different situations. For instance, experimental data suggests that extremely low-angle impacts could result in significant vaporization that would be restricted to the outer layer of the planet [52], due to a phenomenon known as jetting [39], which is not well duplicated by hydrocodes. It may also be possible to reach a similar outcome through a series of high-velocity impacts by more moderate size impactors, for which the smaller isobaric cores would limit the depth from which material would be included in a vapor plume. In both of these cases, these are not considered in great depth at this time, since the potential constraint of Mercury’s high

metallic iron to silicate ratio having only been demonstrated [6] for this large scale impacts.

V.2. Iron-Magnesium Differentiation by the Expanding Vapor Plume

This model highlights the importance of the latent heat of vaporization of the most abundant magnesium-silicate phase in the evolution of an expanding vapor plume. The latent heat released by the condensation of the magnesium-rich end-member buffers the temperature of the expanding plume. This causes the thermodynamic path to stay near the initial condensation temperature for several orders of magnitude of expansion beyond an adiabatic expansion that does not account for condensation, as in the first ‘plateau’ seen in Figure 7. Given that magnesium-rich silicates are the dominant constituent of the terrestrial mantles, other phases would likely have negligible effects on the energetics of an expanding parcel. Therefore, this model is a reasonable first order approximation of the local conditions in an impact resulting in a plume initially dominated by mantle-derived vapor.

Moreover, this buffering of the temperature delays the condensation of the iron-silicate end-member (corresponding to the second plateau seen in Figure 7) for a similar extent of expansion. For a relatively wide range of starting entropies, corresponding to a range of at least three orders of magnitude in the molar volume at incipient condensation, the parcel of material reaches the equilibrium criterion with an intermediate fraction of one of the end-member silicate phases condensing. Specifically, our method identifies a range in incipient forsterite condensation from $v_{mol} \sim 10^{-2} - 10^1 \text{ m}^3/\text{mol}$. Silicate vapor expanding under these conditions should result in both a condensate and residual vapor reservoir between which fractionation of elements can occur by the process outlined in Section II.

Comparison of this result to the conditions predicted using the impedance matching technique with M-ANEOS dunite (Figure 10) suggests that impacts with velocities $\gtrsim 25$ km/s should eject a significant volume of vapor in the lower entropy end of this range. This means that moderate levels of compositional modification could occur in impacts, though not as efficiently as impacts with enough velocity to eject a significant amount of material with conditions in the upper part of the entropy range. A rough upper limit on the velocity of impacts involving a large impactor to target mass ratio ($M_{imp}/M_{tar} \sim .1 - .2$) considered in this paper is placed by SPH calculations [4, 6]. Scaling up either parameter above this range considered here to result in disruption of the target body, in these simulations. The

possibility of this more efficient regime of differentiation playing a role in impacts with a smaller impactor is intriguing, both because the bulk or a planet would be able to weather a higher velocity impact from a smaller body, and because the orbital velocity dispersion of smaller bodies would be higher than for larger bodies.

A more detailed chemical model would likely not greatly affect the energetics of these simulations, as the abundance of other condensing phases would be small in comparison to those considered here, and their specific latent heat of vaporization would be similar. The plume behavior demonstrated here translates to a significant amount of expansion, and ultimately the termination of equilibrium condensation of the gas over small changes in temperatures. This should lead to a relatively sharp division between enriched and depleted elements, as those elements which are included into phases that are more refractory than the dominant magnesium-silicate species would be almost completely condensed, and those elements only included in more volatile species would remain almost completely vaporized. Both enrichment and depletion of elements should also proceed in a fashion proportional to the amount of material ejected in the correct entropy range, in a manner similar to that described by the equations 21 and 22 placing bounds on these values. Therefore, relatively similar levels of both enrichment and depletion of elements relative to other terrestrial mantle compositions is a signature that one might look for on Mercury.

A more detailed chemical model is needed to determine whether elements are volatile or refractory in comparison to the abundant magnesium-silicate phase. A comprehensive categorization of elements as relatively refractory or volatile has not been done at these exact conditions. In many cases, it may be similar to the categorization put forward by Lodders 2003 [31] for conditions in the disk. As in Lodders' method, elements might be characterized by their 'host' phases, those phases into which most of that element would be partitioned into. Elements with host phases stable at higher temperatures than forsterite should fall into the enriched category, while elements without such hosts should fall into the depleted group. Elements (such as iron) for which the dominant magnesium-rich phase plays the role of the dominant host would likely have weaker enrichment or depletion trends, as the proportion of ejected materials at a range of intermediate extent of magnesium condensation must be considered. For instance, if the condensation sequence within the plume is similar to that put forward by Lodders 2003, then the differentiation process would be expected lead to enrichment in Al, Ba, Be, Ca, Sc, Ti, V, Sr, Y, Zr, Nb, La, Ce, Pr, Nd, Sm, Eu, Gd,

Tb, Dy, Ho, Er, Tm, Yb, Lu, Hf, Ta, Th and U, since their hosts are silicates that are more refractory than forsterite. The more abundant elements, which under these assumptions, would be depleted are Fe, Mn, Na, P, S, Cl and K. Evidence of enrichment and depletion of some of these may be able to with spectroscopic techniques by MESSENGER, but most require would require samples of Mercury’s for a meaningful analysis.

Condensation of reduced iron is probably not an important process in the system, as it does not condense in favor of fayalite. One could conceive of a case, for a sufficiently iron rich vapor, in which the presence of a second reduced metal phase might play an important role. The details of the condensation would be changed by the inclusion of a forsterite-fayalite solid solution, but even in our end-member case, reduced iron does not condense from an initially silicate starting material. It should be noted, however, that we assumed congruent vaporization of pure mantle silicates in our study, and not cases where there may have initially been a significant amount of reduced iron from the core of the impactor. Such cases may become relevant if there is significant mixing between ejected core and mantle material. This might occur for instance, in an off-axis impact in which the impactor itself has a significant iron core. Consideration of solid solution would likely reach similar results, but with a more continuous transition between the two condensation ‘plateaus’ seen in Figure 7. Thus, for a starting vapor composition resembling that of a moderately iron-rich silicate, our calculations suggest that the only available reservoirs for partitioning are the residual vapor and the condensing silicate. and the relatively simple scenario introduced in Section II is more favorable than a more complicated one with a separate metallic condensed phase.

V.3. Unexplored Parameters

Inhomogeneity of the pre-impact planet might also complicate the determination of a criterion for which this differentiation mechanism might be identified. Under some circumstances, elements concentrated near the surface of the planet might be ejected preferentially to those concentrated in the deep mantle. Such inhomogeneities become more important to the outcome for lower angles of impact, where the roughly spherical energy distribution assumed in Section III is no longer a good approximation. If mixing within the plume is not significant, then such inhomogeneities will also affect the thermochemistry of the local environment within the plume. Radial inhomogeneities are a natural result of crystallization

of a magma ocean which is hypothesized to have existed on Mercury and the other terrestrial planets [18]. The timing of the impact with respect to a magma ocean would change the initial distribution of elements. In the magma ocean, vigorous mixing would make the molten mantle nearly homogenous. Bottom-up crystallization of the magma ocean would then result in a gravitationally unstable compositional profile in which incompatible elements are concentrated near the surface, perhaps under a plagioclase floatation crust [7]. After sufficient time, the mantle will undergo overturn until the phases are sorted such that the more dense ones are located at the bottom of the mantle. Iron rich phases, for example, would be concentrated near the surface prior to overturn and concentrated near the core after overturn. Evaluating the extent to which this inhomogeneity might cause depletion or enrichment of elements, as opposed to the method presented in this paper, would require dynamic simulations of the ejection phase of the impact.

Inhomogeneity could become important in two different ways. First, if the impact ejects material from different depths preferentially, then differentiation based on which elements are concentrated in the ejecta is important. This would be the case for a low-angle impact such as that implicated in the formation of Mars’ crustal dichotomy [3, 33]. Secondly, if elements are concentrated into local environments with composition significantly different from that of a magnesium-rich silicate, then our evaluation of the energetics for these regions may be incorrect as well. The results of our semi-analytic models of energy partitioning through the target also indicate that for impact velocities approaching ~ 30 km/s, there would likely have been significant involvement of the material from the metallic-iron core in portions of the vapor-rich plume. The effect of these more specific cases have not been considered.

Another major uncertainty of the problem is the initial compositions. If the giant impact is to be dominant in determining the bulk mantle composition, then it should be able to reproduce Mercury’s bulk mantle given a starting bulk mantle of the Earth or another terrestrial planet. Although dynamic arguments generally suggest that mixing during the late stages of planetary accretion would homogenize the compositions of the terrestrial planets [11], this process is by definition stochastic and could result in compositional ‘outliers’, especially for smaller bodies. This might include bodies for which fractionation processes occurring at earlier stages of accretion [28, 29, 58] remain more significant. The possibility that both our mechanism and other fractionation mechanisms both led to measurable

changes cannot be ruled out at this time.

It is possible that this differentiation could also be prevalent for smaller impacts, for which individual events would not cause significant bulk mantle changes, but might over a large number of similar events. Such events may in fact lead to more efficient differentiation through this mechanism, since such impacts could have higher impact velocities and, therefore, produce a portion of ejecta sources with higher initial entropies. Since ejecta from such impacts would not penetrate as deeply into the mantle, the importance of preexisting heterogeneities would almost certainly play a larger role. An analysis of these would also rely more heavily on the statistical likelihood of these events, whereas a single stochastic event, as we have considered, need not be a necessarily common event.

V.4. Future Work

Although our methods in their current state do not allow for a satisfactory estimate of the bulk mantle composition following a major impact, we assert that a similar approach could be used to follow the chemical evolution parcels in a simulation of such an impact. The simplest means of doing this would be to run a dynamic simulation (such as SPH [6] or CTH [36]) to some time before condensation begins, and then divide up the model for that particular time step into parcels on which the method presented here could be carried out. This would provide the best understanding of the initial entropy state of the system. Such a study would be complicated by the fact that different parts of the plume reach conditions for condensation at different times, and would therefore require arbitrary choices about how the division of particles was done. Another would be to include a subset of the equations used in this model, which would be evaluated each time step in order to track the fractionation. We have not evaluated the plausibility of modifying either SPH or CTH codes in this way.

The semi-analytical approach used in our estimation of vapor production smoothes over a great deal of the complexities involved with impact plumes, which can eject material by a variety of poorly understood mechanisms including jetting and spallation [39] [52]. While these would be necessary for a full description of the plume, they are likely to involve only small masses compared to the total of ejected material. Our approach is unable to test the effect of even a moderate obliquity on the energy distribution, where the occurrence of a perfect axially-symmetric collision would be exceptionally rare. Further study in this area

would be best served through use of simulations by a hydrocode, such as CTH [36], which are generally thought to handle smaller length scale phenomena better than SPH calculations. Nonetheless, this first step presents our prediction for the energy distribution for the best understood impact parameter.

One major simplification used in this model is the use of separate condensing phases for forsterite and fayalite. A reasonable next step would be to consider the same model with a modification of the equations 9 and 10 used to describe the equilibrium to account for a single solution between the two phases. A similar model is used by Pahlevan and Stevenson 2007 [42]. This would give a more realistic partitioning of iron between the two phases, however, it is unlikely to greatly affect the energetics of the process. The behavior of fayalite at these conditions is still not well constrained by experiments. The data used for all such models involve extrapolation of the thermodynamic properties of the iron end-member from experiments at temperatures well below its vaporization [49]. As a result, there will be a large degree of uncertainty regardless of the complexity of the model. Experimental work [41] on vaporization of olivine does suggest that the qualitative aspect of FeO-rich olivines as being more volatile at the liquid-vapor transition is correct. In order for precise models of this fractionation process, much better experimental constraints on fayalite at these high-temperature, low pressure conditions is necessary. The possible effect of the condensation of a magnesium-rich phase with a more pyroxene-like (higher SiO-MgO ratio) composition is another possibility that might effect both the energetics and chemistry of this process.

A more complex chemical model is necessary to resolve detailed compositional effects of the mechanism. Consideration of additional phases is necessary to determine which elements are enriched by inclusion into refractory phases and which are not. This can be done by making a thermochemical model using compiled thermodynamic data for a diverse group of phases. We attempted to create such a model based on the method described in Lodders 2003 [31], but this type of pure-phase model runs into numerical difficulty when several phases containing the same element are stable or nearly stable, as the equations for the equilibrium coefficients become over-constrained. The major difference we identified between the conditions considered by Lodders and those relevant in a vapor-dominated ejecta plume is that the abundances of the important volatile phases, such as oxygen, which are included by the condensing silicates, can not be assumed to be constant. This seems to be the cause of our difficulties in using their method. The consideration of solutions between

the end-member in this method might resolve this particular problem.

VI. CONCLUSION

In this thesis, we put forward a new mechanism by which differentiation of silicate material might occur during a giant impact. In the ensuing vapor cloud, elements are preferentially partitioned into a condensate or vapor, and remain in a state of incomplete condensation due to the latent heat released through the condensation of an abundant magnesium silicate component. The early-condensing magnesium-rich phases will reaccrete onto the planet, while the iron-rich vapor will be lost via drag. This mechanism is of greatest relevance for the planet Mercury, as its large iron core has been attributed to a giant, hypervelocity impact.

We demonstrate that for significantly energetic ejecta, this mechanism can lead to a depletion of a planet's silicate shell in FeO. We also qualify our models by showing that for an impact of this magnitude a significant volume of shocked material will release to a vapor, and that for nearly on-axis collisions the competing process of pre-existing heterogeneities in the silicate material would be of less significance.

The impact process is one of undeniable importance to the formation of our solar system. This work presents another idea for how impacts may have played an essential role in forming the planets we observe today.

Appendix A: Coupling of Vapor and Liquid Droplets

As droplets condense, they are accelerated by the frictional drag force of the vapor, so that droplets are forced to match the velocity of the vapor after some characteristic time. For the majority of condensation, the system is in the Epstein regime, meaning that the particle size is much less than the mean free path

$$\lambda = \frac{1}{n_v \sigma_p} \quad (\text{A1})$$

where n_v is the number density of vapor molecules and σ_p is the cross section of the droplets. Consider a particle moving with a velocity v relative to a vapor with thermal velocity $c \gg v$.

Molecules impact the ‘downstream’ side of the droplet with a relative velocity $c - v$ and the upstream side with $c + v$. The net momentum transfer is therefore

$$\Delta p = m\pi r^2 [nc(c + v) - nc(c - v)] \quad (\text{A2})$$

resulting in a frictional force

$$F_D \sim \pi r^2 \rho_v c v \quad (\text{A3})$$

where ρ_v is the density of the vapor.

In the limiting case where most of the mass of a given parcel is in the vapor, we get the following relationship from $F = ma$

$$\frac{4}{3}\pi r^3 \rho_o \frac{dv}{dt} = -\pi r^2 \rho_v c v \quad (\text{A4})$$

where ρ_v is the density of the liquid. This allows us to define a timescale for the response of the droplets to the drag force, which is related to the spatial separation that the particles and vapor can obtain.

$$\tau_{rep} = -\frac{v}{dv/dt} \sim \frac{\rho_o r}{\rho_v c} \quad (\text{A5})$$

An order of magnitude estimate for the spatial separation between the slowest and fastest vapor is given by τ_{rep} times the thermal velocity of the vapor.

Appendix B: Equilibrium Criterion

As the vapor plume expands, particles become rarer. The average timescale of a collision between a particular vapor molecule and a condensed droplet is on the order of the mean free path over the thermal velocity. For an order of magnitude approximation of this timescale, one can use the two relevant length scales, that of the droplet r and the vapor plume R/R_o , along with a characteristic velocity, the thermal velocity of the vapor.

$$\begin{aligned} \tau_{col} &\sim \frac{r}{c} \left(\frac{R}{R_o} \right)^3 \\ &\sim \frac{r}{c} \left(\frac{V}{V_o} \right) \end{aligned} \quad (\text{B1})$$

where

$$c = \sqrt{\frac{3k_B T}{\bar{\mu}}} \quad (\text{B2})$$

This timescale also depends on an unknown steric factor, representing the fraction of collisions which result in condensation of a molecule. We assume that this steric factor is close to unity, but it may be significantly lower for the molecular liquid. Experimental investigation is likely necessary to better constrain this.

We define the distance that the plume expands as

$$R - R_o = vt \quad (\text{B3})$$

assuming the expansion of the plume occurs at a constant velocity v . For the radii at which this criterion would become important $R \gg R_o$, thus, the initial radius can be ignored. As a result we can define the characteristic timescale of expansion, τ_R , to be the doubling time of the plume.

$$\tau_R = \frac{R}{v} \quad (\text{B4})$$

For an average particle size on the order of centimeters, this criteria for the cutoff of our equilibrium equations occurs at a degree of expansion of $R/R_o \sim 1000$, corresponding to a volume change $V/V_o \sim 10^9$.

Appendix C: Removal Timescales

The differentiation mechanism described in Section II relies on the difference in timescales between the removal of material of various sizes from the region of space in which it would be reaccreted by the planet. The dominant process for removing the two expected reservoirs of material is different for each reservoir. Vapor molecules are removed relatively quickly by radiation pressure, while condensate particles on the millimeter to centimeter size range would be removed more slowly by Poynting-Robertson drag.

The cross sectional area over which material can be reaccreted can be taken to be the square of the Hill radius

$$R_{hill} = a(1 - e) \left(\frac{m_p}{M_{\text{☿}}} \right)^{\frac{1}{3}} \quad (\text{C1})$$

where a and e are the semi major axis and eccentricity of the orbit, m_p is the mass of the particle and $M_{\text{☿}}$ is the mass of the planet. A familiar form of the radiation pressure is then given by the expression

$$P_{rad} = \frac{4\sigma_B T^4}{3c} \left(\frac{R_{\odot}}{R} \right)^2 \quad (\text{C2})$$

where σ_B is the Stefan-Boltzmann constant, T is the surface temperature of the sun, c is the speed of light, and R/R_{\odot} is the ratio of the orbital radius ($\approx a$) to the radius of the sun. A timescale, τ_{rad} , for removal of a molecule is found by integrating $F = ma$ as follows

$$\ddot{x} = \frac{F_{rad}}{m_{mol}} = \frac{P_{rad}\sigma_{mol}}{m_{mol}} \quad (\text{C3})$$

$$\frac{P_{rad}\sigma_{mol}}{m_{mol}} \frac{\tau_{rad}^2}{2} = x = r_{hill} \quad (\text{C4})$$

$$\tau_{rad} = \left(\frac{2m_{mol}r_{hill}}{P_{rad}\sigma_{mol}} \right)^{\frac{1}{2}} \quad (\text{C5})$$

and solving for time and approximating this as the removal timescale τ_{rad} . Here \ddot{x} is the displacement of a molecule, F_{rad} is the radiation force, m_{mol} is the mass of a molecule and σ_{mol} is the cross section of the vapor molecule.

The relevant force for Poynting-Robertson drag as given by De Pater and Lissauer, 2001 [17] is

$$F_{PR} \approx P_{rad}\sigma_{PR} \left[\left(1 - 2\frac{v_r}{c}\hat{r} \right) - \frac{v_{\theta}}{c}\hat{\theta} \right] \approx -P_{rad}\sigma_{PR}\frac{v_{\theta}}{c}\hat{\theta} \quad (\text{C6})$$

where P_{rad} is equivalent to the radiation pressure introduced previously, σ_{PR} is the cross section of the condensate ‘droplet’, and v_r and v_{θ} are the radial and tangential components of the orbital velocity. Notice that there is a radial component similar the the radiation force for the vapor particle and also a tangential component. This tangential component is the significant term for mm-cm sized particles and can be used to define a timescale τ_{PR} as follows.

$$\Delta R = GM \left(\frac{1}{v_\theta} - \frac{1}{v_{\theta,0}} \right) \quad (\text{C7})$$

$$\Delta v_{\theta} = \sqrt{\frac{GM}{R}} - \sqrt{\frac{GM}{R - R_{\text{hill}}}} = \frac{F_{PR}\tau_{PR}}{m_{PR}} \quad (\text{C8})$$

$$\tau_{PR} = \frac{m_{RPC}}{P_{rad}} \sigma_{RP} \left(1 - \sqrt{\frac{R}{R - R_{\text{hill}}}} \right) \quad (\text{C9})$$

Equation C7 describes the change in radius due to change the decrease in angular momentum of the droplet. Equation C8 describes the decrease in orbital velocity corresponding to that change in orbital radius. The timescale is then defined by the ratio of these quantities with the value for F_{PR} substituted into the equation.

-
- [1] Ahrens, T. J., and J. D. O’Keefe, Impact on the Earth, ocean and atmosphere, *International Journal of Impact Engineering*, 5(1-4), 13–32, 1987.
 - [2] Alemi, A., and D. Stevenson, Why Venus has no moon, in *AAS/Division for Planetary Sciences Meeting Abstracts #38*, *Bulletin of the American Astronomical Society*, vol. 38, p. 491, 2006.
 - [3] Andrews-Hanna, J. C., M. T. Zuber, and W. B. Banerdt, The borealis basin and the origin of the Martian crustal dichotomy, *Nature*, 453(7199), 1212–1215, 2008.
 - [4] Anic, A., Giant collisions in the early solar system, *Dissertation der philosophisch-naturwissenschaftlichen Fakultät Universität Bern*, 2006.
 - [5] Benz, W., W. L. Slattery, and A. G. W. Cameron, Collisional stripping of Mercury’s mantle, *Icarus*, 74(3), 516–528, 1988.
 - [6] Benz, W., A. Anic, J. Horner, and J. A. Whitby, The origin of Mercury, *Space Science Reviews*, 132(2-4), 189–202, 2007.
 - [7] Brown, S. M., and L. T. Elkins-Tanton, Compositions of Mercury’s earliest crust from magma ocean models, *Earth and Planetary Science Letters*, 286(3-4), 446–455, 2009.
 - [8] Cameron, A. G. W., The partial volatilization of Mercury, *Icarus*, 64(2), 285–294, 1985.
 - [9] Canup, R., and E. Asphaug, Origin of the Moon in a giant impact near the end of the Earth’s formation, *Nature*, 412(6848), 708–712, 2001.
 - [10] Chambers, J. E., Making more terrestrial planets, *Icarus*, 152(2), 205–224, 2001.

- [11] Chambers, J. E., Planetary accretion in the inner solar system, *Earth and Planetary Science Letters*, 223(3-4), 241–252, 2004.
- [12] Chambers, J. E., and G. W. Wetherill, Making the terrestrial planets: N-body integrations of planetary embryos in three dimensions, *Icarus*, 136(2), 304–327, 1998.
- [13] Chase, M. W., N. I. of Standards, M. Technology (Gaithersburg, and J. A. N. A. Force, *NIST JANAF Thermochemical Tables 1 Al - Co*, American Inst. of Physics [u.a.], Woodbury, NY, 1998.
- [14] Croft, S. K., A first-order estimate of shock heating and vaporization in oceanic impacts, *Tech. Rep. (A84-25651 10-42)*, Geological Society of America, 1982.
- [15] Denevi, B. W., and M. S. Robinson, Mercury’s albedo from mariner 10: Implications for the presence of ferrous iron, *Icarus*, 197(1), 239–246, 2008.
- [16] Denevi, B. W., M. S. Robinson, S. C. Solomon, S. L. Murchie, D. T. Blewett, D. L. Domingue, T. J. McCoy, C. M. Ernst, J. W. Head, T. R. Watters, and N. L. Chabot, The evolution of Mercury’s crust: A global perspective from MESSENGER, *Science*, 324(5927), 613–618, 2009.
- [17] DePater, I., and J. J. Lissauer, *Planetary sciences*, 528 pp., Cambridge University Press, Cambridge ; New York, 2001.
- [18] Elkins-Tanton, L. T., E. M. Parmentier, and P. C. Hess, Magma ocean fractional crystallization and cumulate overturn in terrestrial planets: Implications for Mars, in *Meteoritics and Planetary Science*, vol. 38, pp. 1753–1771, 2003.
- [19] Fegley, B., and A. G. W. Cameron, A vaporization model for iron silicate fractionation in the Mercury protoplanet, *Earth and Planetary Science Letters*, 82(3-4), 207–222, 1987.
- [20] Frey, H., and R. Schultz, Large impact basins and the mega-impact origin for the crustal dichotomy on Mars, *Geophysical Research Letters*, 15(3), 229–232, 1988.
- [21] Grossman, L., Condensation in primitive solar nebula, *Geochimica et Cosmochimica Acta*, 36(5), 597, 1972.
- [22] Hart, S. R., and A. Zindler, In search of a bulk-Earth composition, *Chemical Geology*, 57(3-4), 247–267, 1986.
- [23] Hutson, M. L., A. M. Ruzicka, and D. W. Mittlefehldt, The case against Mercury as the angrite parent body (APB), *Meteoritics and Planetary Science Supplement*, 42, 5238, 2007.
- [24] Irving, A. J., S. M. Kuehner, D. Rumble, T. E. Bunch, and J. H. Wittke, Unique angrite nwa 2999: The case for samples from Mercury, *AGU Fall Meeting Abstracts*, p. A898, 2005.

- [25] Jeanloz, R., D. L. Mitchell, A. L. Sprague, and I. de Pater, Evidence for a basalt-free surface on Mercury and implications for internal heat, *Science*, *268*(5216), 1455–1457, 1995.
- [26] Kraus, R. G., S. T. Stewart, D. C. Swift, C. A. Bolme, R. Smith, S. Hamel, B. Hammel, D. K. Spaulding, D. G. Hicks, J. H. Eggert, and G. W. Collins, Shock induced vaporization of silica: Implications for giant impact events, in *Lunar and Planetary Science Conference (42nd)*, 2011.
- [27] Lawrence, D. J., W. C. Feldman, J. O. Goldsten, L. G. Evans, N. R. Izenberg, L. Nittler, E. A. Rhodes, and S. C. Solomon, Combining MESSENGER neutron spectrometer data from Mercury flybys 1 and 3: Estimates of the global concentration of neutron-absorbing elements on Mercurys surface, *AGU Fall Meeting Abstracts*, p. D7, 2009.
- [28] Lewis, J. S., Metal/silicate fractionation in the solar system, *Earth and Planetary Science Letters*, *15*(3), 286–290, 1972.
- [29] Lewis, J. S., Temperature-gradient in solar nebula, *Science*, *186*(4162), 440–443, 1974.
- [30] Lisse, C. M., Abundant circumstellar silica dust and SiO gas created by a giant hypervelocity collision in the 12 Myr hd172555 system, *The Astrophysical Journal*, *701*(2), 2019, 2009.
- [31] Lodders, K., Solar system abundances and condensation temperatures of the elements, 2003.
- [32] Margot, J. L., S. J. Peale, R. F. Jurgens, M. A. Slade, and I. V. Holin, Large longitude libration of Mercury reveals a molten core, *Science*, *316*(5825), 710–714, 2007.
- [33] Marinova, M. M., O. Aharonson, and E. Asphaug, Mega-impact formation of the Mars hemispheric dichotomy, *Nature*, *453*(7199), 1216–1219, 2008.
- [34] McClintock, W. E., N. R. Izenberg, G. M. Holsclaw, D. T. Blewett, D. L. Domingue, J. W. H. III, J. Helbert, T. J. McCoy, S. L. Murchie, M. S. Robinson, S. C. Solomon, A. L. Sprague, and F. Vilas, Spectroscopic observations of Mercury’s surface reflectance during MESSENGER’s first Mercury flyby, *Science*, *321*(5885), 62–65, 2008.
- [35] Mcdonald, J. E., Homogeneous nucleation of vapor condensation .2. kinetic aspects, *American Journal of Physics*, *31*(1), 31, 1963.
- [36] McGlaun, J., S. Thompson, and M. Elrick, CTH - a 3-dimensional shock-wave physics code, *International Journal of Impact Engineering*, *10*(1-4), 351–360, 1990.
- [37] Melosh, H. J., *Impact cratering : a geologic process*, 245 pp., Oxford University Press; Clarendon Press, New York; Oxford, 1989.
- [38] Melosh, H. J., A new and improved equation of state for impact computations, in *Lunar*

- and Planetary Institute Science Conference Abstracts, Lunar and Planetary Institute Science Conference Abstracts*, vol. 31, p. 1903, 2000.
- [39] Melosh, H. J., and C. P. Sontt, When worlds collide: Jetted vapor plumes and the Moons origin, *Tech. rep.*, Lunar and Planetary Institute, 1984.
 - [40] Mitchell, D. L., and I. de Pater, Microwave imaging of Mercury’s thermal emission at wavelengths from 0.3 to 20.5 cm, *Icarus*, *110*(1), 2–32, 1994.
 - [41] Nagahara, H., I. Kushiro, and B. O. Mysen”, Evaporation of olivine: Low pressure phase relations of the olivine system and its implication for the origin of chondritic components in the solar nebula, *Geochimica et Cosmochimica Acta*, *58*(8), 1951, 1994.
 - [42] Pahlevan, K., and D. J. Stevenson, Equilibration in the aftermath of the lunar-forming giant impact, *Earth and Planetary Science Letters*, *262*(3-4), 438–449, 2007.
 - [43] Palme, H., and B. Fegley, High-temperature condensation of iron-rich olivine in the solar nebula, *Earth and Planetary Science Letters*, *101*(2-4), 180–195, 1990.
 - [44] Pierazzo, E., and H. J. Melosh, Understanding oblique impacts from experiments, observations, and modeling, *Annual Review of Earth and Planetary Sciences*, *28*, 141–167, 2000.
 - [45] Pierazzo, E., A. M. Vickery, and H. J. Melosh, A reevaluation of impact melt production, *Icarus*, *127*(2), 408–423, 1997.
 - [46] Raizer, Y. P., Condensation of a cloud of vaporized matter expanding in a vacuum, *Soviet Physics JETP*, *37*(6), 1741–1750, 1960.
 - [47] Ribas, I., E. F. Guinan, M. Gadel, and M. Audard, Evolution of the solar activity over time and effects on planetary atmospheres. i. high-energy irradiances, *The Astrophysical Journal*, *622*(1), 680, 2005.
 - [48] Riner, M. A., F. M. McCubbin, P. G. Lucey, G. J. Talyor, and J. J. Gillis-Davis, Mercury surface composition: Integrating petrologic modeling and remote sensing data to place constraints on FeO abundance, *Icarus*, *209*, 301–313, 2010.
 - [49] Robie, R., and B. Hemingway, Thermodynamic properties of minerals and related substances at 298.15 k and 1 bar (10^5 pascals) pressure and at higher temperatures, *U.S. Geol. Survey Bull.*, vol. *2131*, p. *461-461 (1995).*, *2131*, 461–461, 1995.
 - [50] Robinson, M. S., and G. J. Taylor, Ferrous oxide in Mercury’s crust and mantle, *Meteoritics and Planetary Science*, *36*(6), 841–847, 2001.
 - [51] Salpeter, E. E., Nucleation and growth of dust grains, *Astrophysical Journal*, *193*(3), 579–584,

- 1974.
- [52] Schultz, P. H., Effect of impact angle on vaporization, *Journal of Geophysical Research-Planets*, 101(E9), 21,117–21,136, 1996.
 - [53] Smith, D. E., M. T. Zuber, R. J. Phillips, S. C. Solomon, G. A. Neumann, F. G. Lemoine, S. J. Peale, J. L. Margot, M. H. Torrence, M. J. Talpe, J. W. Head, S. A. Hauck, C. L. Johnson, M. E. Perry, O. S. Barnouin, R. L. McNutt, and J. Oberst, The equatorial shape and gravity field of Mercury from MESSENGER flybys 1 and 2, *Icarus*, 209, 88–100, 2010.
 - [54] Sprague, A., J. Warell, G. Cremonese, Y. Langevin, J. Helbert, P. Wurz, I. Veselovsky, S. Orsini, and A. Milillo, Mercury’s surface composition and character as measured by ground-based observations, in *Space Science Reviews*, pp. 399–431, Springer, 2007.
 - [55] Tonks, W. B., and H. J. Melosh, Core formation by giant impacts, *Icarus*, 100(2), 326–346, 1992.
 - [56] Tonks, W. B., and H. J. Melosh, Magma ocean formation due to giant impacts, *Journal of Geophysical Research-Planets*, 98(E3), 5319–5333, 1993.
 - [57] Tyler, A. L., R. W. H. Kozlowski, and L. A. Lebofsky, Determination of rock type on Mercury and the Moon through remote sensing in the thermal infrared, *Geophysical Research Letters*, 15(8), 808–811, 1988.
 - [58] Weidenschilling, S. J., Iron-silicate fractionation and origin of Mercury, *Icarus*, 35(1), 99–111, 1978.
 - [59] Zel’dovich, I. A. B., and I. U. P. Raïzer, *Physics of shock waves and high-temperature hydrodynamic phenomena*, 916 pp., Mineola, N.Y. : Dover Publications, c2002., 2002.